U.S. DEPARTMENT OF ENERGY | Office of Science

DOE/SC-ARM-TR-297

TRACER Radar b1 Data Processing: Corrections, Calibrations, and Processing Report

Y-C Feng
M Rocque
T Wendler
E Schuman
V Castro
S Collis
A Theisen
A Matthews
M Deng
K Johnson
I Lindenmaier
SE Giangrande
R Jackson
J Comstock

March 2024

ARM

DISCLAIMER

TRACER Radar b1 Data Processing: Corrections, Calibrations, and Processing Report

Y-C Feng, Pacific Northwest National Laboratory (PNNL)
A Matthews, PNNL
M Rocque, PNNL
M Deng, Brookhaven National Laboratory (BNL)
T Wendler, PNNL
K Johnson, BNL
E Schuman, PNNL
I Lindenmaier, PNNL
V Castro, PNNL
SE Giangrande, BNL
S Collis, Argonne National Laboratory (ANL)
R Jackson, ANL
A Theisen, ANL
J Comstock, PNNL

March 2024

How to cite this document:

Feng, Y-C, A Matthews, M Rocque, M Deng, T Wendler, K Johnson, E Schuman, I Lindenmaier, V Castro, SE Giangrande, S Collis, R Jackson, A Theisen, and J Comstock. 2024. TRACER b1 Data Processing: Corrections, Calibrations, and Processing Report. U.S. Department of Energy, Atmospheric Radiation Measurement user facility, Richland, Washington. DOE/SC-ARM-TR-297.

Work supported by the U.S. Department of Energy,
Office of Science, Office of Biological and Environmental Research

Acronyms and Abbreviations

ADP	attenuation-corrected differential reflectivity
AMF	ARM Mobile Facility
ANL	Argonne National Laboratory
ARM	Atmospheric Radiation Measurement
ARSCL	Active Remote Sensing of Clouds Value-Added Product
BNL	Brookhaven National Laboratory
CCOR	clutter power correction
CMS	clutter micro-suppression
CPA	clutter phase alignment
CSAPR	C-band Scanning ARM Precipitation Radar
CSU	Colorado State University
DOE	U.S. Department of Energy
DQR	Data Quality Report
DSD	disdrometer
GE	general sensitivity
GOES	Geostationary Operational Environmental Satellites
HOU	Houston, Texas
HSRHI	hemispherical range height indicator
IOP	intensive operational period
KaSACR	Ka-band Scanning ARM Cloud Radar
KAZR	Ka-band ARM Zenith
KDP	specific differential phase
LD	laser disdrometer
LDQUANTS	Laser Disdrometer Quantities Value-Added Product
LDR	linear depolarization ratio
LNA	low-noise amplifier
M1	main facility
MD	chirp moderate sensitivity
mRCA	modified relative calibration adjustment
PHIDP	differential phase
PI	principal investigator
PNNL	Pacific Northwest National Laboratory
PPI	plan position indicator
PyART	Python ARM Radar Toolkit
RCA	relative calibration adjustment

RCS	radar cross-section
RF	radio frequency
RHI	range height indicator
RhoHV	co-polarization correlation coefficient
RR	rain rate
RWP	radar wind profiler
SACR	Scanning ARM Cloud Radar
SACRCOR	Scanning ARM Cloud Radar Corrections Value-Added Product
SNR	signal-to-noise ratio
SNRh	signal-to-noise ratio at horizontal polarization
SQI	signal quality index
TRACER	Tracking Aerosol Convection Interactions Experiment
UTC	Coordinated Universal Time
VAP	value-added product
VDIS	video disdrometer
VDISQUANTS	Video Disdrometer Quantities Value-Added Product
VPT	vertically pointing
Vr	absolute radial velocity
WRA	wet radome attenuation
XSACR	X-band Scanning ARM Cloud Radar
ZDR	differential reflectivity

Contents

Figures

Tables

1.0 Introduction

The U.S. Department of Energy (DOE) Atmospheric Radiation Measurement (ARM) user facility deployed the first ARM Mobile Facility (AMF1) to Houston, Texas for the Tracking Aerosol Convection Interactions Experiment (TRACER) field campaign. The TRACER campaign was conducted from October 1, 2021 to September 30, 2022, with an intensive operational period (IOP) from June 1 to September 30, 2022.

To investigate the life cycles of convective cells in the polluted and humid urban environment of Houston, ARM deployed cloud and precipitation radars, including the C-band Scanning ARM Precipitation Radar (CSAPR2), the X/Ka-band Scanning ARM Cloud Radar (SACR), and the Ka-band ARM Zenith cloud Radar (KAZR), as shown in Figure 1. This report presents an analysis of radar data quality, hardware calibrations, and radar data corrections.

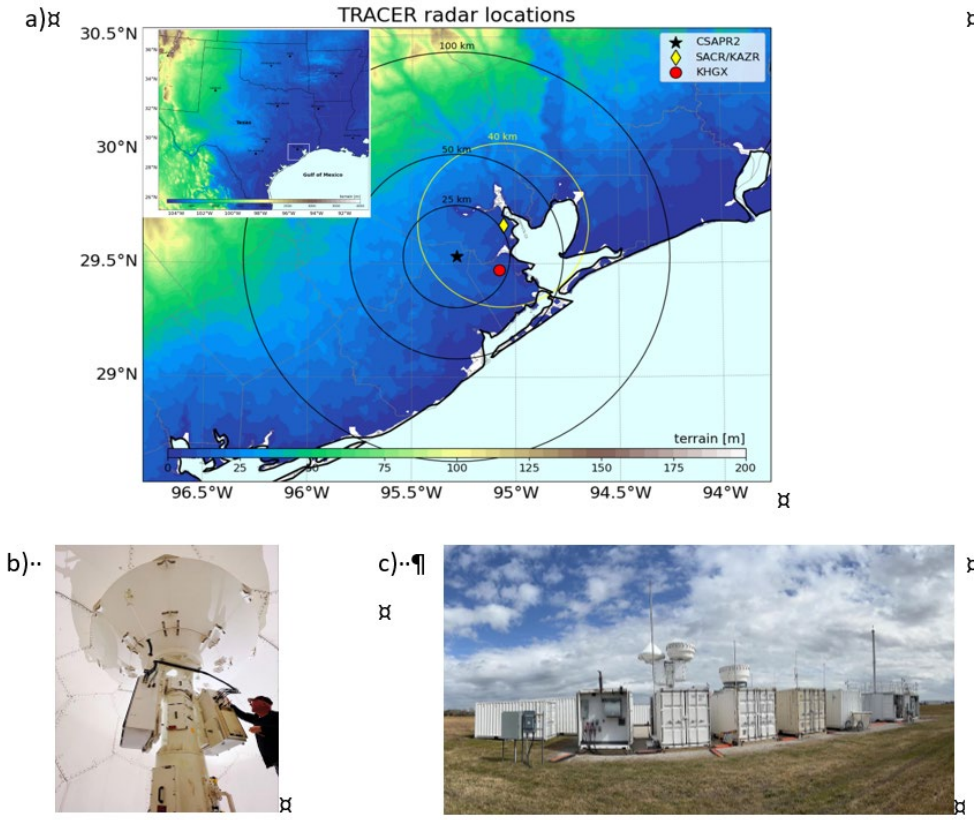

Figure 1. a) The deployments of ARM radars (CSAPR2: black star, SACR and KAZR: yellow diamond) during TRACER. Range rings for CSAPR2 at 25, 50, and 100 km are shown in black and the SACR range ring at 40 km in yellow. The WSR-88D KHGX radar is marked as a red dot. SACR and KAZR are collocated at the main facility (M1). CSAPR is located at the S2 site. Terrain heights (m) are shaded; the insert depicts the southern U.S. for context. b) Images of CSAPR2 during normal maintenance. c) Cloud radars, from left to right: XSACR with a cone-shaped radome, KaSACR with a slanted radome, and KAZR. (Photo: Vagner Castro.)

1.1 TRACER ARM Radar Settings and Scan Strategy

Table 1 outlines the specifications of the ARM precipitation and cloud radars. Table 2 summarizes the scanning strategy employed by CSAPR2 and X/Ka SACR. Typically, a standard scanning strategy is scheduled at regular 10-minute intervals and includes plan position indicator (PPI), vertically pointing (VPT), and hemispherical range height indicator (HSRHI) scans. The radar filenames are labeled with the 'HOU' site code, and the scan type can be identified through the "scan_name" and "scan_mode" parameters in the files.

During TRACER, an adaptive cell-tracking method was implemented in CSAPR2. The cell-tracking scanning strategy, operated by the principal investigators (PIs), is designed to investigate the evolution of convective cells with high temporal resolution (Lamer et al. 2023). Targeted cell-tracking scans typically include three low-level sector PPI scans, followed by one to six range height indicator (RHI) scans across targeted convective cells focusing on maximum reflectivity and polarimetric variable fields. The combined volume scans span a duration of two to three minutes and continue to follow the targeted cells until a new cell is identified for tracking. These special scans were performed frequently from June 2022 to October 2022 during the IOP on convective days. Cell-tracking files can be distinguished by the "template_name" parameter within the a1-data files, which has the term "cell-track". For example, a file with a "template_name" like "hou-rhi-cell-track-25-deg" indicates a cell-tracking RHI scan spanning 25 degrees in elevations, while "hou-ppi-cell-track-30-deg" indicates a cell-tracking PPI scan covering 30 degrees in azimuth. The number after "cell-track" varies depending on scan areal coverage of the PI's designs.

Table 1. ARM radar specifications during TRACER.

Radar	Frequency (GHz)	Polariza-tion	Transmit power (kW)	Antenna diameter (m)	Beam-width (deg)	Gate spacing (m)	Maximum range (km)	Nyquist velocity (m/s)
CSAPR2	5.7	Dual	350	4.3	0.9	100	100	16.5
XSACR	9.73	Dual	1.7	1.8	1.25	25	25, 40 (Change after Mar 22)	17.8
KaSACR	35.3	Single	2	1.82	0.33	25		5.3, 8 (after Jul 12)
KAZR	34	Single	0.187	2	0.3	29.98	25	8

Table 2. The conventional scanning strategy deployed during TRACER.

Radar	Site	PPI: ° in elevations	VPT	HSRHI: ° in azimuth, from -90° to 90° in elevation	Heartbeat, including PPI, VPT, HSRHI scans	Special scans
CSAPR2	S2	0.5, 1.5, 3	VPT	Saved in two files, (54, 84, 114, 144, 174, 204) and (63 over M1)	10 min	Cell tracking, contains a few PPIs and RHIs
X-Ka SACR	M1	1, 2	VPT	0, 30, 60, 90, 120, 150	10 min	

1.2 Radar Operation Performances

The operational periods for radars during TRACER are depicted in Figures 2 and 3. The KAZR operation was notably stable with a high data collection rate. CSAPR2 encountered hardware issues in the early period of TRACER but was operational effectively for the majority of the IOP. Therefore, the CSAPR2 data from April 20 onwards are considered operational and are processed at the b1 level. Data between November 23 to April 20, 2022, is at the a1 level documented with a Data Quality Report (DQR), but no b1-level corrected data files are provided. Data discontinuity in Figures 2 and 3 are likely affected by factors such as hardware maintenance, the replacement of malfunctioning components, radar calibration procedures, or radar malfunction induced by lightning. All the a1 and b1 data can be downloaded from ARM's Data Discovery and plots generated from a1-level data can be viewed on ARM's DQplotbrowser.

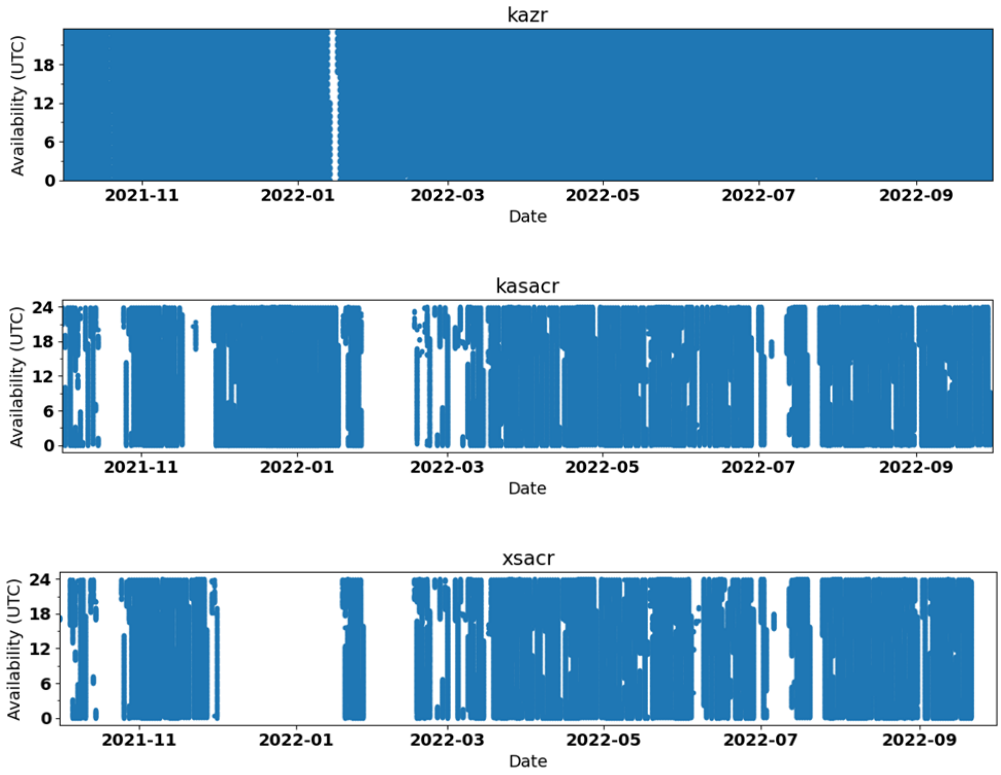

Figure 2. Radar data availability for KAZR, KaSACR, and XSACR.

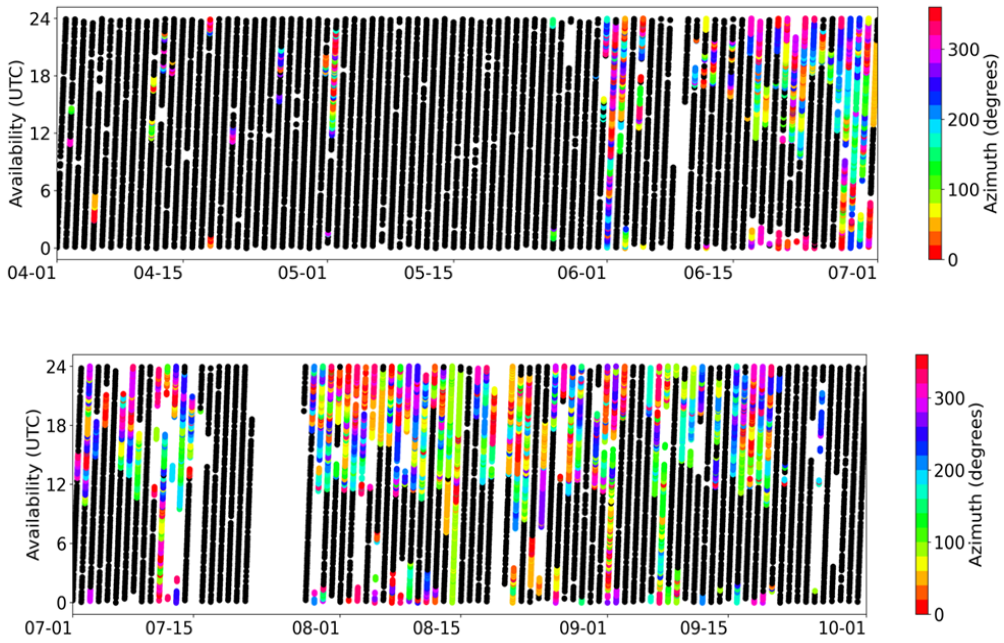

Figure 3. The data availability of CSAPR2 from April to October 2022. X-axis is the date and time in UTC (local time equals UTC - 6 hours). Regular scans are indicated by black dots. Cell-tracking scans are represented by colored dots, where different colors correspond to the azimuthal focus of cells. Most of the cell-tracking scans were performed during daytime. Since there are a huge number of data files, particularly during cell-tracking periods, the files are plotted every six files.

1.3 b1 Data Processing

The purpose of the b1 data processing is to provide high-quality calibrated radar data for quantitative scientific applications. The current b1-level data processing primarily focuses on correcting reflectivity-related fields and applying masks to filter out non-hydrometeor signals.

1.3.1 Radar Calibration and Data Corrections

The quality of reflectivity measurements is affected by the performance and stability of the radar system. The radar equation can be expressed as

$$Z = P_r + C + 20\,log10(r)$$

where Z is the logarithmic expression for radar reflectivity factor in dBZ, P_r is the received power in dBm, r is the range in kilometers, and C is the logarithmic radar constant in dB.

The challenge in radar calibration lies in determining the radar constant C. The radar constant C is a function of radar system parameters and physical constants, including transmitted power, receiver gain, antenna beamwidth, signal pulse length, dielectric factor, and so on. Changes in these system factors, such as fluctuations in transmitted power or waveguide losses, can induce a change in C over time and subsequently impact the accuracy of Z. Consequently, maintaining a well-calibrated radar system requires regular testing for the factors of the radar system to obtain stable and accurate C.

The primary objective in radar calibration is to obtain an accurate determination of *C*. Various methods have been developed to obtain accurate measurements of *C* for calibration. Conventionally, engineers perform laboratory calibrations, corner reflector calibrations, or solar calibrations in the field to calibrate the radar system factors of *C* and to monitor the stability of the radar system. During the initial phase of TRACER, the engineering and technician team conducted some of these calibrations (see Appendix A for more details). However, due to limited staffing, some engineering calibrations such as corner reflector calibration were performed infrequently. Moreover, the radar constant is determined based on known radar system parameters and considerations of radar-related issues. During radar operations, unforeseen hardware malfunctions or environmental factors, such as high temperature and humidity, can also influence radar performance. Therefore, to ensure stable data quality, we primarily rely on the post-data analyses outlined below for data corrections in the b1-level radar data.

Several post-data-processing methodologies can be applied to assess the stability of a radar system, estimate radar systematic biases for data corrections, and analyze uncertainties. These methods include the relative calibration adjustment (RCA) technique using ground clutter, self-consistency of polarimetric variables, and intercomparison with other overlapping reliable, calibrated instruments such as disdrometers or other collocated radars. These methods and analyses will be further discussed in Section 2. The practice of using reliable measurements from overlapping calibrated data, typically assumed to be a truth reference, is commonly referred to as radar adjustment. The mean biases resulting from cross-comparisons can be designated as radar calibration bias, considering spatiotemporal resolution sampling differences, scattering regimes, radome conditions (dry, wet, or with water streaks), and hydrometeor advection due to wind conditions.

1.3.2 Data Quality Masks

Radars receive signals not only from hydrometeors but also from ground clutter, insects, birds, extraneous radio sources at the same frequency, etc. Distinguishing between these non-meteorological echoes and genuine weather signals is essential for accurately interpreting atmospheric data and deriving accurate hydrological products. During TRACER, the frequently observed non-meteorological features are listed in Table 3. In the b1 data, the non-hydrometeor masks vary among radars and depend on the measured parameters. These non-meteorological signals are identified and discussed in the b1-data process to help the data users exclude the non-weather-related information.

However, non-hydrometeor signals are not inherently without value. Some of these non-meteorological signals can be useful for various purposes. For example, fixed ground targets can be used for examining radar stability. Fine lines of the reflectivity fields caused by insects can be used for identifying the daytime sea-breeze front boundaries or boundary-layer convective rolls prior to convection initiation, or storm cold pool outflows. Examples are illustrated in the following sections.

Table 3. Frequent non-meteorological signals observed during TRACER.

CSAPR2	Extraneous radio frequency (RF) interferences; south-side tree beam blockage; biological signals such as insects, birds, bats; second trips
SACR	Radio frequency interferences, second-trip issues, biological signals, ground clutter
KAZR	Biological signals

2.0 Methodology for Radar Data Correction

Several factors are considered when the b1-level reflectivity (Z) and differential reflectivity (ZDR) corrections are determined including systematic hardware issues, attenuation due to hydrometeors or gas, and the wet-radome effect. Thus, the standard a1-to-b1 radar data process focuses on

1) correcting the biases of Z and ZDR, and providing data uncertainty analysis:

$$Z_{b1\_corrected} = Z_{a1} + Z_{system\_bias} + Z_{attenuation}$$
$$ZDR_{b1\_corrected} = ZDR_{a1} + ZDR_{system\_bias} + ZDR_{attenuation}$$

2) masks for non-meteorological signals

The methodologies used to achieve these goals depend on the capabilities of radar polarizations, the availability and reliability of surrounding instruments, and the environmental conditions during TRACER. This section introduces the data calibration methodologies in Section 2, and the radar data bias analyses for each radar in Section 3. A summary of the corrections applied is shown in Table 4.

Table 4. b1-data correction summary list. Linear fits for KAZR GE and MD modes are applied during the later period, where t represents time (days) in the linear fit in the figures below.

	CSAPR2	XSACR	KASACR	KAZR GE	KAZR MD
Z_{system_bias} (dB)	+1.2	+3.2	10/1/21 – 3/20/22: -0.4 3/21/22 – 10/1/22: +2	10/1/21 – 6/30/22: +1 7/1/22 – 8/31/22: 0.07*t + 1.9 9/1/22 – 10/1/22: -0.19*t+ 8.58	10/1/21 – 11/8/21: +2.5 11/9/21 – 6/30/22: +2.1 7/1/22 – 8/31/22: 0.05*t + 3.73 9/1/22 – 10/1/22: -0.31*t + 9.46
ZDR_{system_bias} (dB)	0.67	0.2 from May to Sep, +2.46 from Sep 2-4	N/A	N/A	N/A
KDP	Y	Y	N/A	N/A	N/A
Attenuation	Hydrometeor attenuation for $Z_{attenuation}$, $ZDR_{attenuation}$		Gas attenuation in c-level		
Mask	Y	Y	Cloud censor mask	Cloud censor mask	Cloud censor mask

2.1 Reflectivity Bias Estimation and Correction: Z_{system_bias}

2.1.1 Relative Calibration Adjustment (RCA)

For scanning radars, RCA is a simple but powerful method to monitor the reflectivity stability in time and provide the relative reflectivity calibration in operational radars. Reflectivity of strong ground clutter within close range of a radar generally shows high values and stability with small fluctuations of less than 0.5 dB (Silberstein et al. 2008, Wolff et al. 2015, Hunzinger et al. 2020). Changes greater than 1 dB in the daily mean Z from clutter are usually related to issues with the radar system. Hence, we apply RCA to assess the stability of the radar and provide an initial Z calibration for the SACR in TRACER. RCA is not applied for CSAPR2 during TRACER because the collected reflectivity is filtered and processed with a ground-clutter-removal algorithm built into the radar's signal processing.

The conventional RCA is defined as, RCA = Z95_baseline - Z95_daily, where Z95_baseline is the 95th percentile baseline Z of ground clutter and Z95_daily is a daily 95th Z of ground clutter (Wolff et al. 2015). If the daily reflectivity is lower than the baseline reflectivity of the ground targets, RCA is positive, which suggests we need to add the RCA values to the Z for correction; and vice versa.

In TRACER, the RCA methodology is modified. The Z95_baseline is calculated as the mean of a selected period where Z95_daily had stable radar status. The modified RCA (mRCA) is then calculated as: mRCA = Z95_baseline_mean - Z95_daily. Ground targets are selected within the range of 1.5 to 9.5 km from SACR. Additionally, the criteria for selecting ground targets includes Z > 30 dBZ, absolute radial velocity (Vr) < 0.3 m/s, and co-polarization correlation coefficient (RhoHV) < 0.5. The RhoHV threshold is only applied for XSACR.

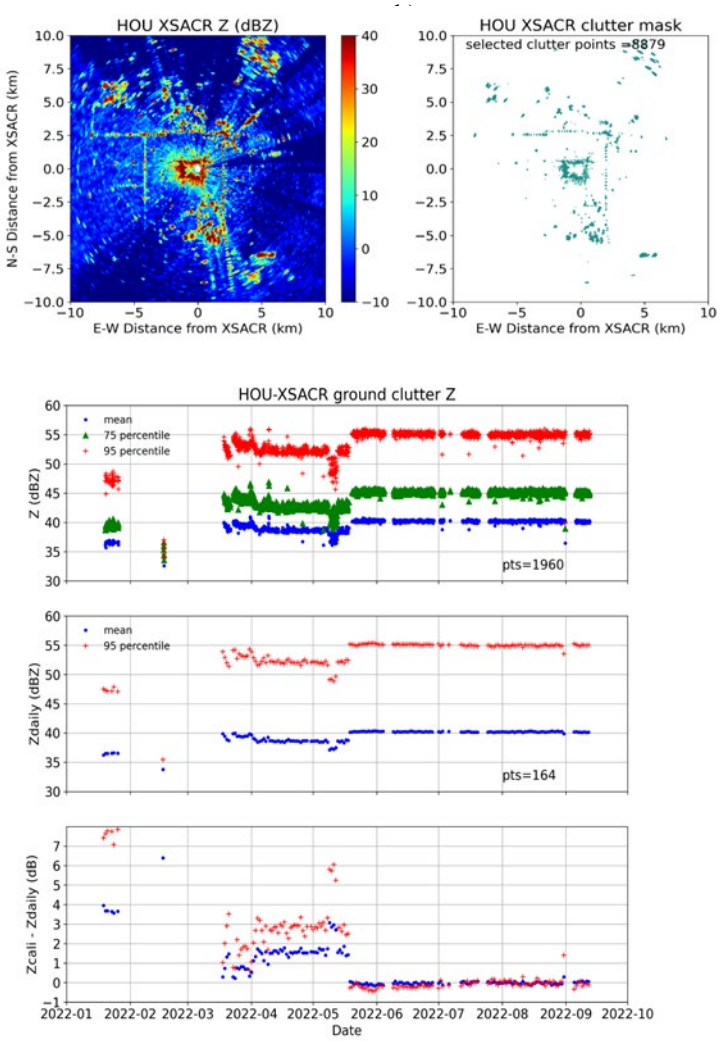

Figure 4. a) The HOU XSACR reflectivity field at 1° elevation on a clear day. b) The identified ground clutter used for the RCA and radar stability monitoring. c) Mean (blue dots), 75th (green triangles), and 95th (red cross) percentiles of ground clutter reflectivity distributed for HOU XSACR. d) Daily mean of c). The Z_baseline_means are highlighted in the transparent thick lines. e) mRCA (dB). Zcali in the plot corresponds to the Z95_baseline_mean.

Figure 4 shows the selected ground targets near XSACR, primarily consisting of structures such as buildings or lamp poles rather than terrain. The Z_daily value is consistent from March to early May and from May 20 to September 11, indicating stable radar performance during these periods. XSACR was turned off in the middle of September, resulting in no available data thereafter. The data before March is not compared to the latter two stable periods due to unstable hardware and coarser azimuthal resolution during that timeframe.

In May, the changes of Z_daily were attributed to the change of the RF, leading to a slight decrease in Z_daily by 2-3 dB. Following the replacement of the RF during May 17-20, Z_daily exhibited improved stability. There is a ~3 dB change for the 95th percentile of selected targets, and a ~2 dB change for the mean of selected targets. The second stable period from May to September is determined to be the calibration period (Z95_baseline). The daily mean values (standard deviation) of the Z_baseline_95th and Z_baseline_mean are 55 dBZ (0.4 dB) and 40 dBZ (0.16 dB), respectively.

In Figure 5, the KaSACR Z_daily is within 1 dB variation from April to October, showing the stability of KaSACR. The baseline period of mRCA is selected from April to July. The mean values (standard deviation) of Z95_baseline_mean and Zmean_baseline are 46.1 dBZ (0.6 dB) and 37.2 dBZ (0.36 dB), respectively. Since the total number of selected ground targets of KaSACR (166 points) is much less than XSACR (8879 points), which is related to the smaller beam width of KaSACR, we suggest applying mRCA_mean instead of mRCA_95th. Averaging with more samples enhances the reliability and reduces the fluctuation for the relative calibration applications.

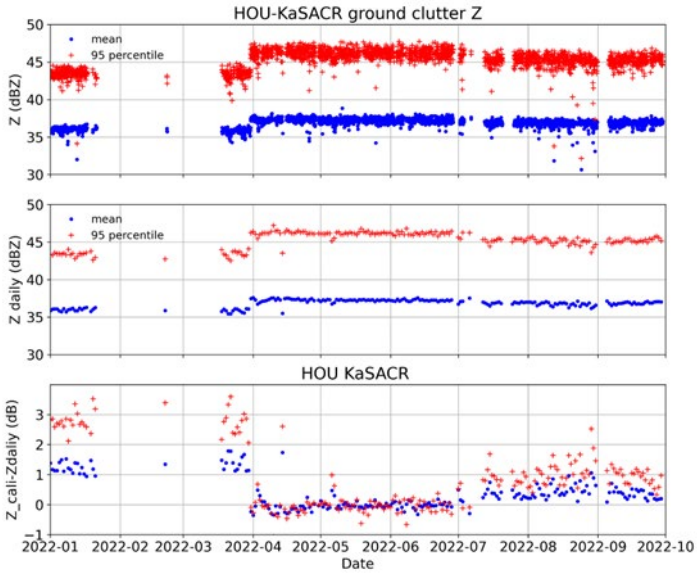

Figure 5. Same as Figure 4 c) to e), but for KaSACR.

2.1.2 Cross-Comparison between ARM Radars and other Calibrated Instruments

To estimate reflectivity bias, a cross-comparison is conducted between ARM radars, the WSR-88D KHGX radar, and disdrometers. The availability of cross-comparison instruments in TRACER is listed in Table 5. Cross-comparison thresholds for the Z (Table 6) are set under conditions of Rayleigh scattering

for both radars and with no hydrometeor attenuation. Figure 6 shows the relationship between the attenuation reflectivity (A_H) and the reflectivity at different radar frequencies. It illustrates the Z values at the onset of hydrometeor attenuation, serving as the upper boundary for comparison between different frequency of radars. For single polarization, such as KaSACR, $A_H = a*Z_H^b$ is used, where Z_H is reflectivity in linear units of mm^6m^{-3}. The coefficients for these attenuation equations were derived from the ARM Laser Disdrometer Quantities Value-Added Product (LDQUANTS VAP; Hardin et al. 2020), where Z and ZDR can be simulated using laser disdrometer data through T-matrix scattering models.

Table 5. The locations and data collection periods of neighboring instruments used to perform the cross-comparison with the ARM radars.

Instrument – site	Longitude	Latitude	Height (ASL)	Data collection periods
CSAPR2 – S2	-95.284	29.532	12m	20220401-20220930
SACR, KAZR – M1	-95.059	29.67	8 m	20211001-20220930
WSR-88D – KHGX	-95.0787	29.4719		all TRACER period
Disdrometer – M1 (houvdisquantsM1)	-95.059	29.67	8 m	20190427-20220929
Disdrometer – M1 (houldquantsM1)	-95.059	29.67	8 m	20200526-20220930
Disdrometer – S1 (houldquantsS1)	-95.059	29.67	8 m	20190422-20221001
Disdrometer – S2	-95.284	29.532	12m	20220412-20220512
RWP – M1	-95.059	29.67	8 m	20190813-20210310
RWP – S2	-95.284	29.532	12 m	20210304-20220919

Table 6. Thresholds for cross-comparison between radars.

	Z range (dBZ)	SNR	Range	Correlation coefficient minimum
KHGX vs XSACR	10 to 35	N/A	< 2 km (VPT)	> 0.985
XSACR vs KASACR	-5 to 15	> 0	< 2 km (VPT)	> 0.985
KASACR vs KAZR	-5 to 15	> 0	None, testing < 2 km	N/A
KAZR GE vs MD	-5 to 15	> 0	N/A	N/A

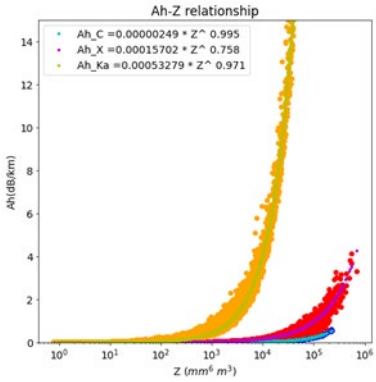

Figure 6. The relationship between Ah and Z with C-, X-, and Ka-band radars.

2.1.3 Self-Consistency Method

The self-consistency method relies on the relationship between Z, ZDR, and specific differential phase (KDP). This dual-polarimetric variable relationship is established through the analysis of drop size distributions from disdrometers and T-matrix scattering models. By applying the Z-ZDR-KDP relationship along with calibrated ZDR and derived KDP values, we can estimate theoretical Z values. Then, after accounting for the hydrometeor attenuation of Z, the Z_{system_bias} can be determined by comparing the theoretical Z with the measured Z. Figure 7 shows that the Z_{system_bias} of CSAPR2 obtained from the self-consistency method is around 1.2 dB. Then, $Z_{b1\_corrected} = Z_{a1} + Z_{attenuation} + Z_{system\_bias}$.

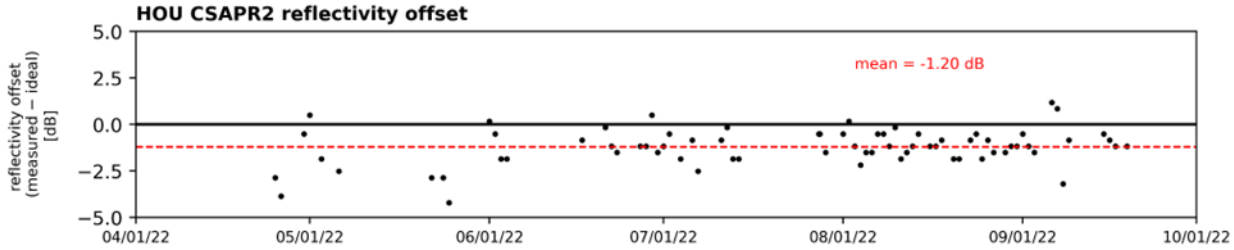

Figure 7. Time series of CSAPR2 daily mean differences between measured and ideal reflectivity using the self-consistency method before any corrections are applied. Plotted days have at least 1000 points. The mean of the daily means is -1.2 dB.

2.2 Differential Reflectivity (ZDR) Correction: ZDR_{system_bias}

ZDR calibration is performed through VPT scans during light rain events. Under such conditions, the average ZDR values of small spherical raindrops along a full 360 degrees averaging are expected to be 0 dB. This is based on the theory that the axis ratio of the small drop is expected to be 1, resulting in a ZDR value close to 0 dB.

For CSAPR2, the daily ZDR mean from VPT scans under light rain is consistently around -0.67 dB from April 2022 until the end of September 2022 (Figure 8a). Thus, the ZDR b1 data is corrected by adding 0.67 dB to the ZDR a1 data.

For XSACR, ZDR_{system_bias} is around 0.2 dB from May to September 2022 (Figure 8b). Yet, the ZDR_{system_bias} values abruptly change to -2.46 dB during September 2 to 4. This abrupt change in ZDR is possibly related to the wet-radome effect of successive fixed vertically pointing scans. For the corrected ZDR b1 data, 0.2 dB is added to the ZDR a1 data from May through September, except for reducing 2.46 dB in the beginning of September.

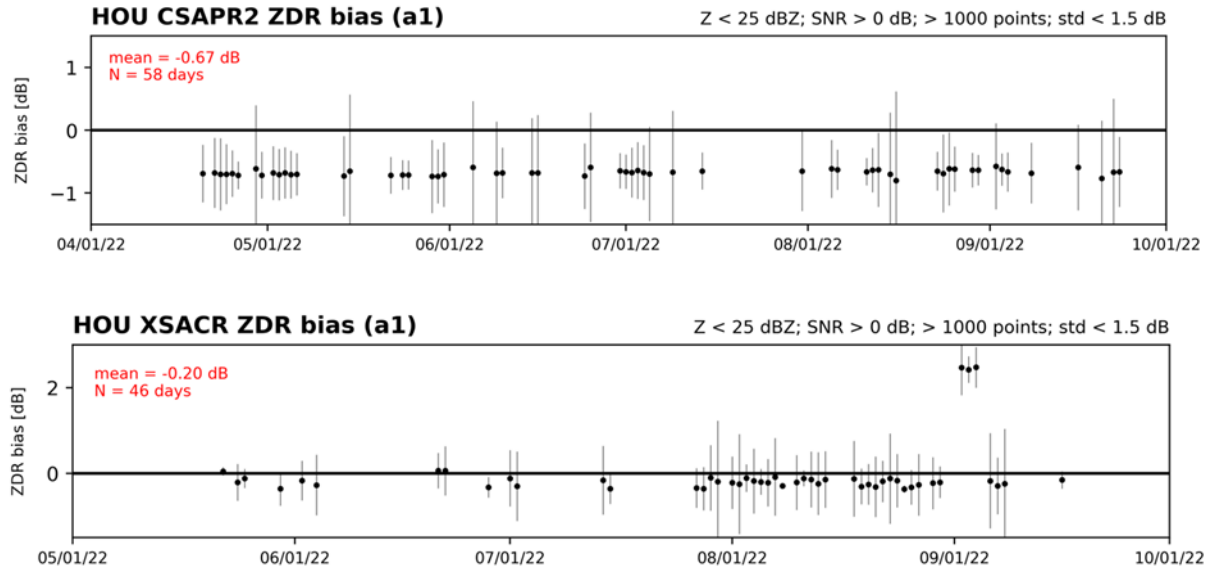

Figure 8. Time series of daily ZDR bias estimation of CSAPR2 and XSACR. Dots and error bars represent the daily mean and standard deviation, respectively. The ZDR_bias in the plot is calculated as ZDR_a1 – ZDR_bias = ZDR_b1.

2.3 Attenuation Correction of Hydrometeors ($Z_{attenuation}$ and $ZDR_{attenuation}$) and KDP Calculation

The attenuation of reflectivity and differential reflectivity by rain is considerable for higher-frequency radars, particularly during heavy rainfall in the summer in Houston. For CSAPR2 and XSACR with dual-polarization capabilities, the specific attenuation and specific differential attenuation, A_H and A_{DP}, can be estimated from a fitted relationship with KDP: $A_H = c^* KDP^d$, $A_{DP} = e^* KDP^f$ (Figure 9). Based on these equations, the path-integrated attenuation can be estimated and added back to the a1 data for correction. Path-integrated attenuation is accumulated in range and counted in both directions (two-way). The KDP is derived from the differential phase (PHIDP) data using the CSU_RadarTools open-source module (calc_kdp_bringi; Hubbert and Bringi 1995). Based on these equations, the path-integrated attenuation can be corrected.

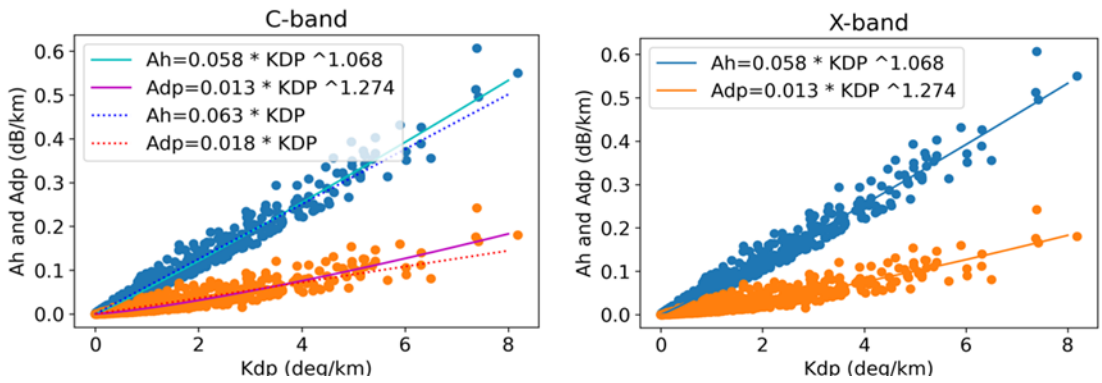

Figure 9. The relationship between Ah and A_{DP} versus KDP for C-band and X-band radars, respectively.

2.4 Gas Attenuation

In the humid Houston area, considering gas attenuation by water vapor is crucial. Figure 10 depicts the time series of gas attenuation over a vertical column for the KAZR at TRACER. Gas attenuation values at the farthest range of KAZR range from 0.1 to 1.2 dB, depending on the temporal moisture change. For KaSACR, the gas attenuation is more pronounced in the horizontal direction as the range increases. The gas attenuation of KAZR and KaSACR is not corrected in the current b1 data flow. Following established conventions, this correction will be applied in the c1 Active Remote Sensing of Clouds (ARSCL) VAP data for KAZR and SCANNING ARM CLOUD RADAR CORRECTIONS (SACRCOR) VAP for KaSACR. In the b1 processing, gas attenuation estimations serve a role in estimating uncertainties for the reflectivity cross-comparison analyses.

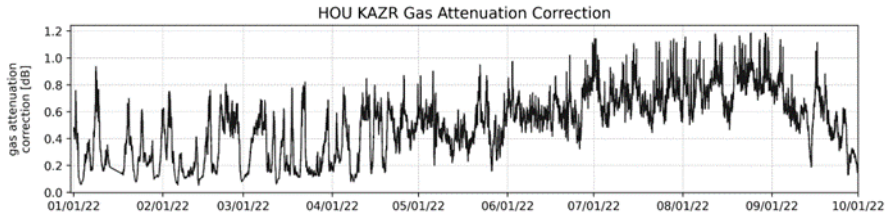

Figure 10. Time series of the gas attenuation correction of reflectivity for KAZR.

3.0 TRACER Radar b1 Correction

3.1 CSAPPR2 b1 Data Process

For CSAPR2 b1 data, Z and ZDR are corrected based on the following concept:

$$Z_{b1\_corrected} = Z_{a1} + Z_{attenuation\_hydrometeors} + Z_{system\_bias}$$
$$ZDR_{b1\_corrected} = ZDR_{a1} + ZDR_{attenuation\_hydrometeors} + ZDR_{system\_bias}$$

Here are the detailed steps:

i. Estimate KDP for attenuation correction of $ZDR_{attenuation\_hydrometeors}$ and $Z_{attenuation\_hydrometeors}$ using the A_{DP} – KDP and A_H – KDP relationships, respectively (Figure 9).
ii. Estimate ZDR_{system_bias}, which is 0.67 dB, from VPT scans (Figure 8a).
iii. Obtain $ZDR_{b1\_corrected}$ by correcting $ZDR_{attenuation\_hydrometeors}$ and ZDR_{system_bias}.
iv. Estimate Z_{system_bias}, which is 1.2 dB, using the $ZDR_{b1\_corrected}$, KDP, and Z with attenuation corrections, self-consistency method (Figure 7).
v. Obtain $Z_{b1\_corrected}$ by correcting the $Z_{attenuation\_hydrometeors}$ and Z_{system_bias} values.

The self-consistency method for Z_{system_bias} was applied to provide a consistent evaluation for CSAPR2 across both conventional and storm-tracking scans. Additionally, some limited CSAPR2 a1 reflectivity fields with conventional scans were compared with the data from the WSR-88D KHGX radar, the radar wind profiler (RWP), and the disdrometers for preliminary data quality evaluation. Figure 11a shows the reflectivity intercomparison between CSAPR2 a1 VPT data and the KHGX Z profiles over the CSAPR2 site below 1 km. CSAPR2 Z is 0.86 dB lower than KHGX Z, while the attenuation is relatively small, making attenuation nearly negligible in the vertical direction with the Z ranging from 5 to 35 dBZ. This result closely aligns with the Z_{system_bias} estimated from the self-consistency method. Yet, the correlation is only 0.73 due to the limited number of conventional scans and the temporal resolution of VPT scans being approximately 10 minutes, which is insufficient to fully compensate for the hydrometeor advection effect in various wind conditions. For example, Figure 11b presents a time series of Z comparison between CSAPR2 and other instruments on April 24 and 25, suggesting that Z may vary case by case depending on factors such as precipitation type, convection or stratiform, and rain rates. To increase the number of samples, one can also analyze the overlapping areas between CSAPR2 and KHGX PPI scans. Figure 12 shows the Z intercomparison using CSAPR2 a1 PPI scans and KHGX PPI scans. On average, CSAPR2 is 2.9 dB lower than KHGX during selected cases for April 24-25, May 22, and September 3, 2022. The Z difference varies across different cases, as the difference includes the same Z_{system_bias} but varying $Z_{attenuation\_hydrometeors}$ due to different rainfall intensities.

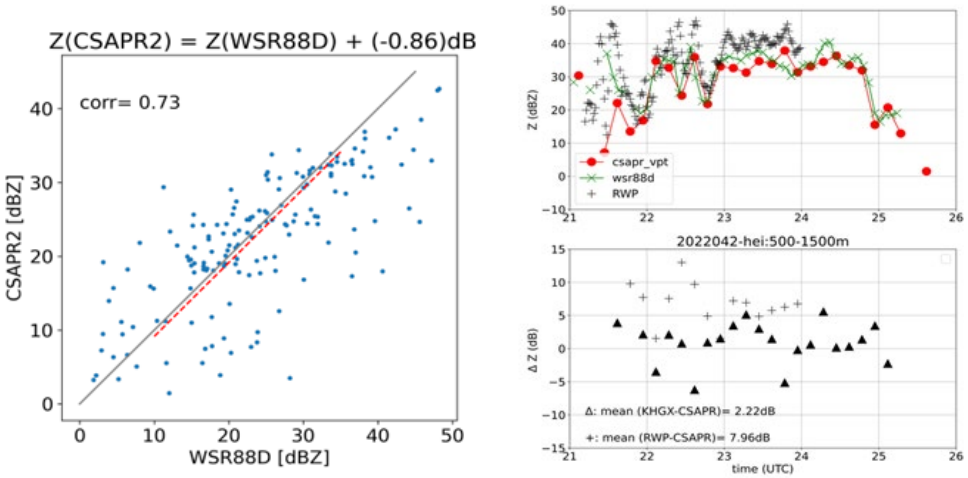

Figure 11. a) Comparison of Z values below 1-km height between CSAPR2 a1 data and WSR-88D KHGX data shown as blue dots. The red dashed line is the linear fit between the CSAPR2 a1 and KHGX to estimate the offset with less (can be ignored) hydrometeor attenuation. b) The time series comparison of reflectivity between the CSAPR2 a1-level VPT, WSR-88D, and the calibrated RWP on April 25.

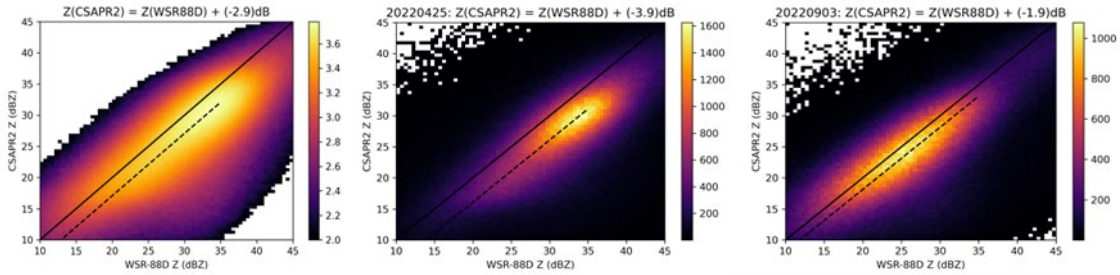

Figure 12. The PPI Z comparison between WSR-88D KHGX and CSAPR2 for all cases (left), for a case with heavier rainfall on April 25 (middle), and lighter rainfall on September 3 (right). Color shading represents the total counts at log10 scale (left). The code to extract overlapping data from PPI scans is available in the Python ARM Radar Toolkit (PyART) Gate Mapper function.

3.1.1 Data Examples

Figure 13c provides a comprehensive visualization of the correction states of Z and ZDR in a convective storm of a cell-tracking scan (Figure 13 a,b), along with the KDP estimations, offering insights into the transformation of key parameters throughout the process. The a1-level to b1-level processing for Z and ZDR includes corrections for systematic bias and hydrometeor attenuation. As depicted in the figure, the attenuation corrections for Z and ZDR increase with range, particularly beyond the KDP column, reaching up to 3 deg/km at distances of 35-40 km from the radar. This is just one example of a convective cell observed during TRACER. Multiple high-temporal RHI scans are available, particularly during cell-tracking periods (Figure 3). These scans provide valuable opportunities to investigate microphysical processes with high temporal and vertical resolutions, including the evolution of ZDR and KDP columns, cloud-top growth, etc.

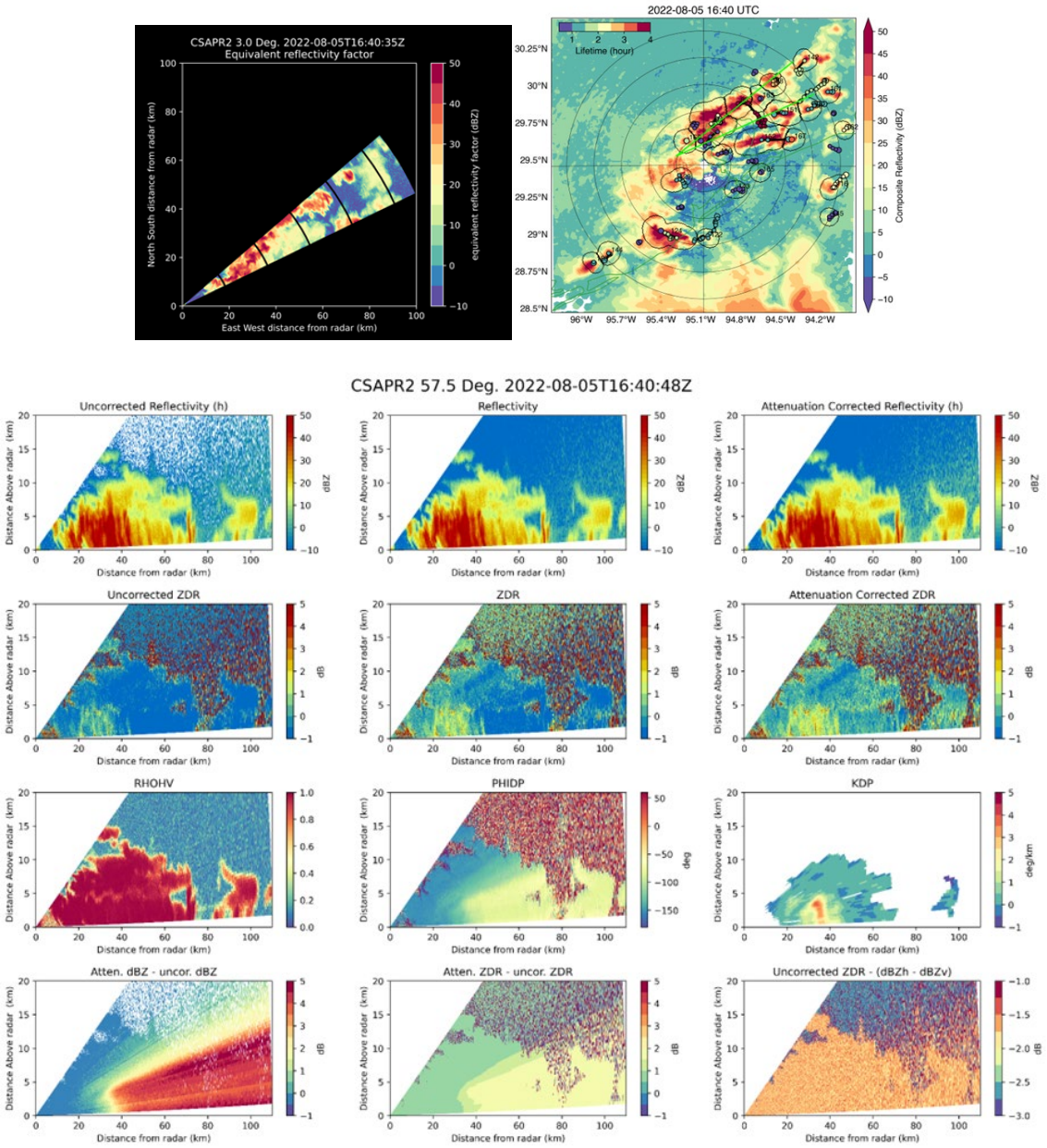

Figure 13. An example of cell-tracking scans, containing the sector PPI and RHI scans. a) selected PPI scans to targeted cells. b) WSR88D radar composite with cell identifications and tracking shown as dots and circles methods using PyFLEXTRKR (Feng et al. 2022) provided by Dr. Ye Liu. The CSAPR2 cell-tracking direction is highlighted with the lime-colored lines. c) a1 to b1 process flow for Z and ZDR. (First row) Z correction process from a1 to b1 level, including a1-level uncorrected Z, corrected Z with systematic bias, and b1-level corrected Z incorporating both systematic bias and attenuation correction. (Second row) ZDR correction from a1 to b1 with the correction level like the Z process. (Third row) dual-polarization fields from left to right: correlation coefficient (RhoHV), differential phase shift (PHIDP), and derived specific differential phase (KDP) at b1-level. (Fourth row) The attenuation correction for Z and ZDR, as well as the raw Zh-Zv.

3.1.2 Masks

Two masks generated by the CSAPR2 processing system are available in the b1 data: the censor mask and the classification mask. Censor and classification masks are available for PPI, RHI, and HSRHI scans. An example of the censor and classification masks applied to a PPI and an RHI from TRACER is shown in Figure 14.

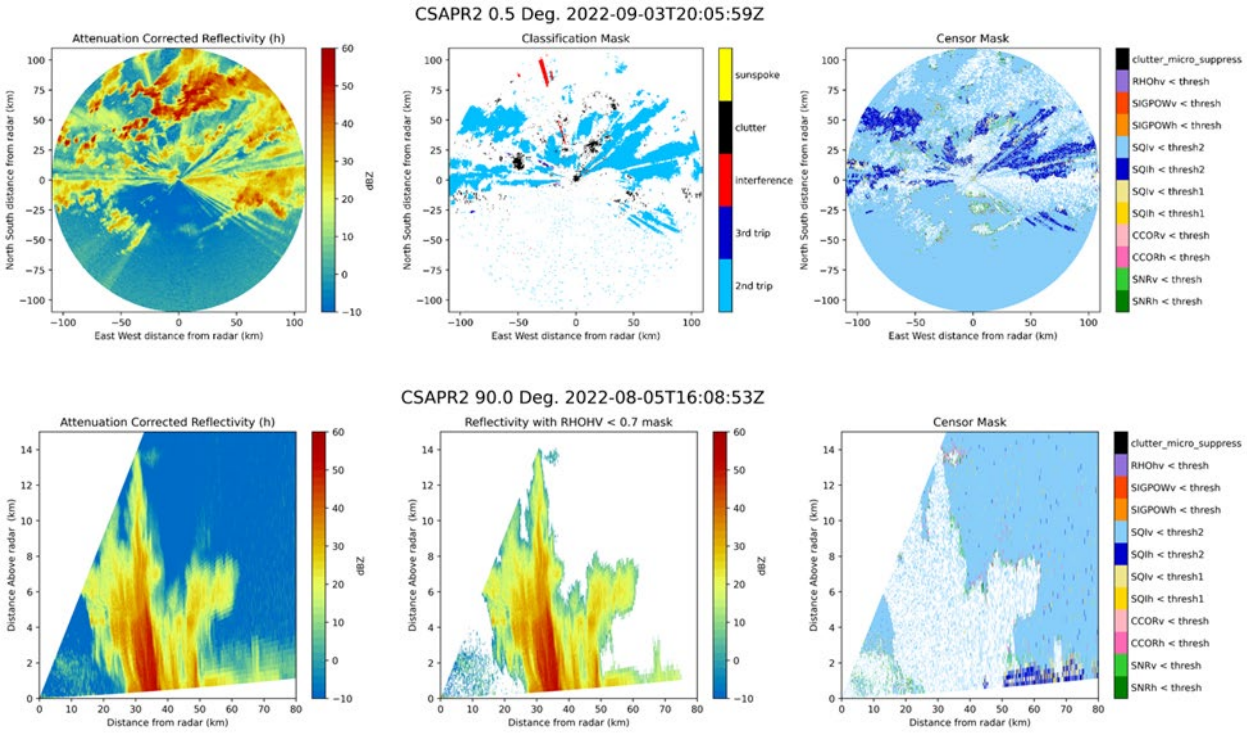

Figure 14. (top) CSAPR2 0.5° PPIs of attenuation-corrected reflectivity (dBZ), classification mask, and censor mask at 2005 UTC on 3 September 2022. (bottom) CSAPR2 90° RHIs of attenuation-corrected reflectivity (dBZ), reflectivity with RhoHV threshold, and censor mask at 1608 UTC on 5 August 2022.

- **The classification mask** has five flags: second trip, third trip, interference, clutter, and sun spoke. The classification mask for cell-tracking RHIs in the TRACER data set only outputs 'clutter' flags and thus should not be used. We suggest users apply a threshold of RhoHV < 0.7 to mask additional non-meteorological signals.
- **The censor mask** has 12 flags. Clutter is identified using several variables including signal-to-noise ratio (SNR), clutter power correction (CCOR), clutter micro-suppression (CMS), and clutter phase alignment (CPA). CPA is a measure of the phase variability of the received signal with values closer to 1 indicating a higher probability of clutter. Second- and third-trip signal quality index (SQI) values are calculated and compared with first-trip SQI values to determine if echoes are actually second/third trip. Gates are classified as interference if the SQI is low, and the standard deviation of normalized power is high. If there is a high percentage of gates along a ray that meet the criteria for interference (> 75%), they are classified as a sun spoke. A list of these flags and the default thresholds used by the signal processor is shown in Table 7.

Table 7. CSAPR2 censor mask values, descriptions, and default thresholds.

Censor Mask		
Value	**Description**	**Default Thresholds**
1	Signal-to-noise ratio at horizontal polarization (SNRh) below noise threshold	0.5 dB
2	SNRv below noise threshold	
4	Clutter power correction (CCORh) below CCOR threshold	-30 dB
8	CCORv below CCOR threshold	
16	Signal quality index (SQIh; normalized coherent power) below SQI1 threshold	0.4
32	SQIv below SQI1 threshold	
64	SQIh below SQI2 threshold	0.5
128	SQIv below SQI2 threshold	
256	Signal power (SIGPOWh) below SIGPOW threshold	10 dB
512	SIGPOWv below SIGPOW threshold	
1024	RhoHV below RhoHV threshold	0.8
2048	Censored by Clutter Micro-Suppression (CMS)	40 dB

3.2 X-Ka SACR Data Correction

For XSACR b1 data, Z and ZDR are corrected with the following concept:

$$Z_{b1\_corrected} = Z_{a1} + Z_{attenuation\_hydrometeors} + Z_{system\_bias}$$

$$ZDR_{b1\_corrected} = ZDR_{a1} + ZDR_{attenuation\_hydrometeors} + ZDR_{system\_bias}$$

For KaSACR b1 data, Z correction is as:

$$Z_{b1\_corrected} = Z_{a1} + Z_{system\_bias} (+ Z_{attenaution\_gas})$$

In the following discussion, our emphasis is on estimating Z_{system_bias} for both XSACR and KaSACR. The corrected values of $ZDR_{attenuation\_hydrometeors}$ and ZDR_{system_bias} of XSACR have already been described in Section 2. The gas attenuation values of KaSACR will be corrected in the VAP c-level radar data following conventional practices.

3.2.1 Z Comparison between WSR-88D KHGX and ARM Radar Sets

We use WSR-88D KHGX to assess the Z_{system_bias} of XSACR under specific conditions. Then, the corrected XSACR $Z_{b1\_corrected}$ will be used to estimate the Z_{system_bias} of KaSACR through radar data intercomparison.

Columns over the XSACR were taken from KHGX data using the PyART columnsect utility. Next, to ensure the radars were seeing similar points, both data sets were filtered to include only points where RhoHV was greater than 0.985, Z was between 10 and 35 dBZ, and the height was less than 2 km. XSACR data was additionally filtered with an SNR > 0 dB. Comparisons for the XSACR focused on data after May 20, 2022, because prior to this date the XSACR had hardware issues. The RF unit was replaced

on May 18, 2022, there after significantly improving data quality. This comparison, shown in Figure 15, exhibits high case-to-case variability, but the mean Z_{system_bias} was 3.2 dB.

3.2.1.1 Using KHGX to Correct Z_{system_bias} of XSACR

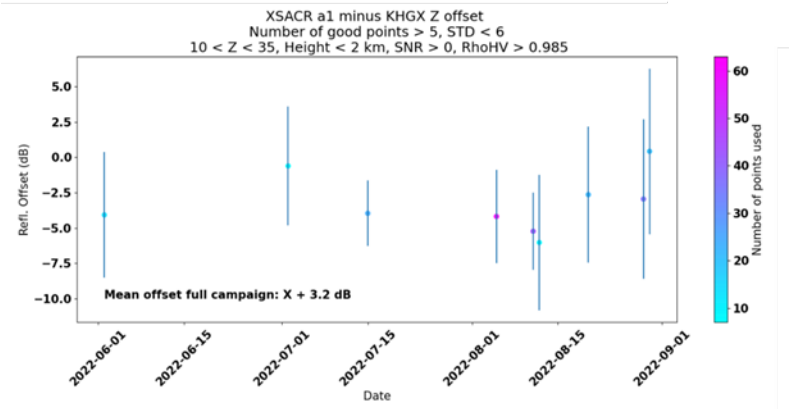

Figure 15. XSACR a1 reflectivity comparison with KHGX.

3.2.1.2 Using Calibrated XSACR to Correct Z_{system_bias} of KaSACR

Now that we have corrected the XSACR reflectivity data, we can use this in comparisons between the XSACR and KaSACR to determine the Z_{system_bias} of the KaSACR. This analysis used vertically pointing data between 500 m and 2 km with SNR values greater than 0 dB and Z values between -5 and 15 dBZ. A filter of RhoHV greater than 0.985 was also applied to the XSACR data only. For the period after the XSACR had the RF unit replaced (May 20) to the end of the campaign, the reflectivity difference was 2 dB, as shown in Figure 16b. Before this date, very few data points pass the filters to use for correction (Figure 16a).

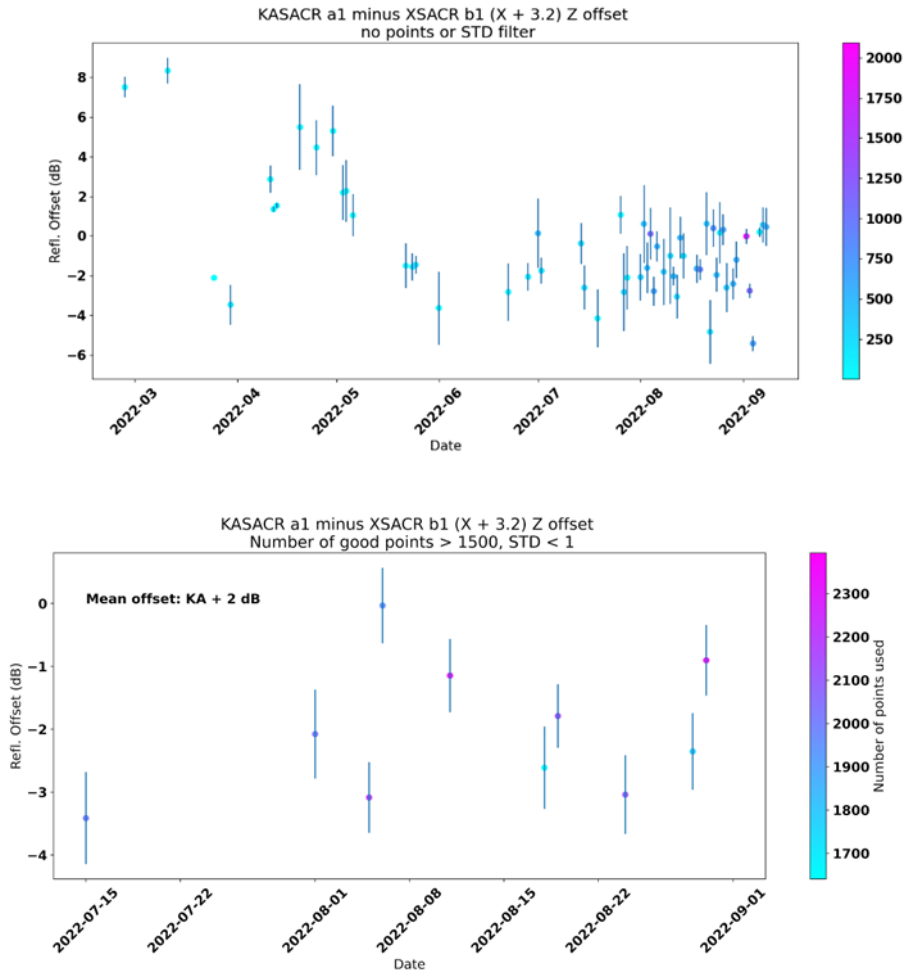

Figure 16. a) KaSACR a1 reflectivity compared to the XSACR b1-level reflectivity showing all data. b) Same as a), but with data filtering using the number of points and the standard deviation.

3.2.2 Z Cross-Comparison with Disdrometers

Disdrometers provide another reliable data set for assessing radar Z performances and Z_{system_bias}. Reflectivity data comparisons were conducted among SACR, KHGX, and the collocated ARM laser disdrometer (LD), as shown in Figure 17. The linear fit between the reflectivity values from radars and the disdrometer shows that Z of KHGX is 3.87 dB lower than Z of LD, and Z_{a1} of XSACR is 7.11 dB lower than Z of LD. For the XSACR and LD comparison, the Z range of 10 to 35 dBZ is considered to eliminate the effect of hydrometeor attenuation. The Z difference between KHGX and the XSACR is 3.24 dB, which is consistent with the comparison between radars in section 2.2.1.1. The same method is also applied using the ARM Video Disdrometer (VDIS) Quantities VAP (VDISQUANTS) and similar Z offsets are observed: KHGX = VDIS - 2.44 dB, XSACR = VDIS - 6.22 dB, KaSACR = VIDS – 8.01 dB.

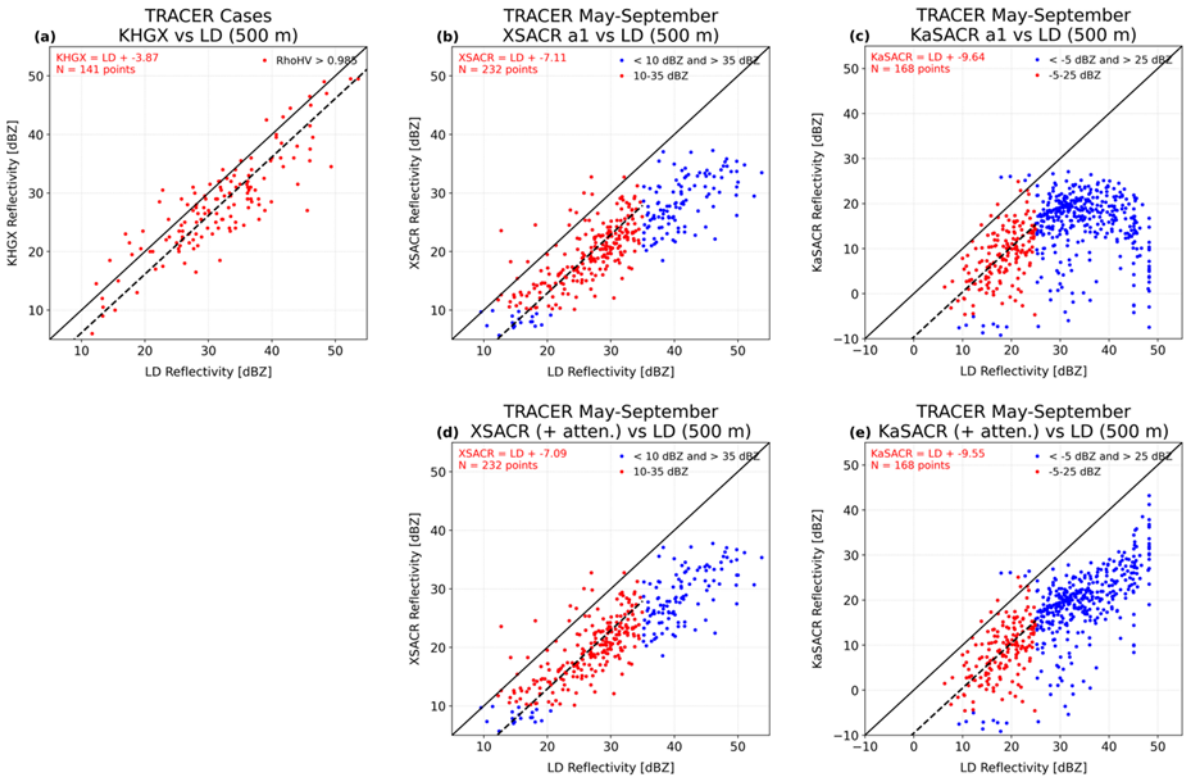

Figure 17. Reflectivity cross-comparisons between the ARM Laser Disdrometer Quantities VAP (LDQUANTS, at x-axis) and radars at y-axis: a) KHGX, b) XSACR, and c) KaSACR, respectively. d-e) Same plots as b and c, but with hydrometeor attenuation corrections.

When Z is over 30 dBZ, the difference between Z_{a1} of KaSACR and Z of LD gradually increases (blue dots in Figure 17c), attributed primarily to hydrometeor attenuation and partially to wet-radome effects. After attenuation correction shown in Figure 17 d and e, the difference between XSACR and LD becomes smaller compared to Figure 17 a,b. The Z difference between XSACR and LD increases with reflectivity and may be attributed from wet-radome effects. For Z below 25 dBZ, the Z_{a1} of KaSACR is 9.6 dB lower than Z of LD within the Z range of 5 to 25 dBZ. This result shows that KaSACR is about 5.7 dB lower the KHGX. In Section 3.2.1, Z_{a1} of KaSACR is 2 dB lower than Z_{a1} of XSACR. The estimations of the KaSACR Z_{system_bias} using LD and using XSACR are about 4 dB difference, potentially related to the sampling difference and assumptions in the simulations matrix of LDQUANTS.

3.2.3 SACR Data Example

Figure 18 shows the transformation of XSACR Z and ZDR data from a1 level to b1 level during deep convection, accompanied by the KDP estimations. Note that PHIDP_0, specifically PHIDP at the first gate, varies in elevation during HSRHI scans, and the reasons for this variation are still under investigation. This PHIDP_0 issue does not impact the KDP estimations, as KDP is derived from the gradient of the PHIDP.

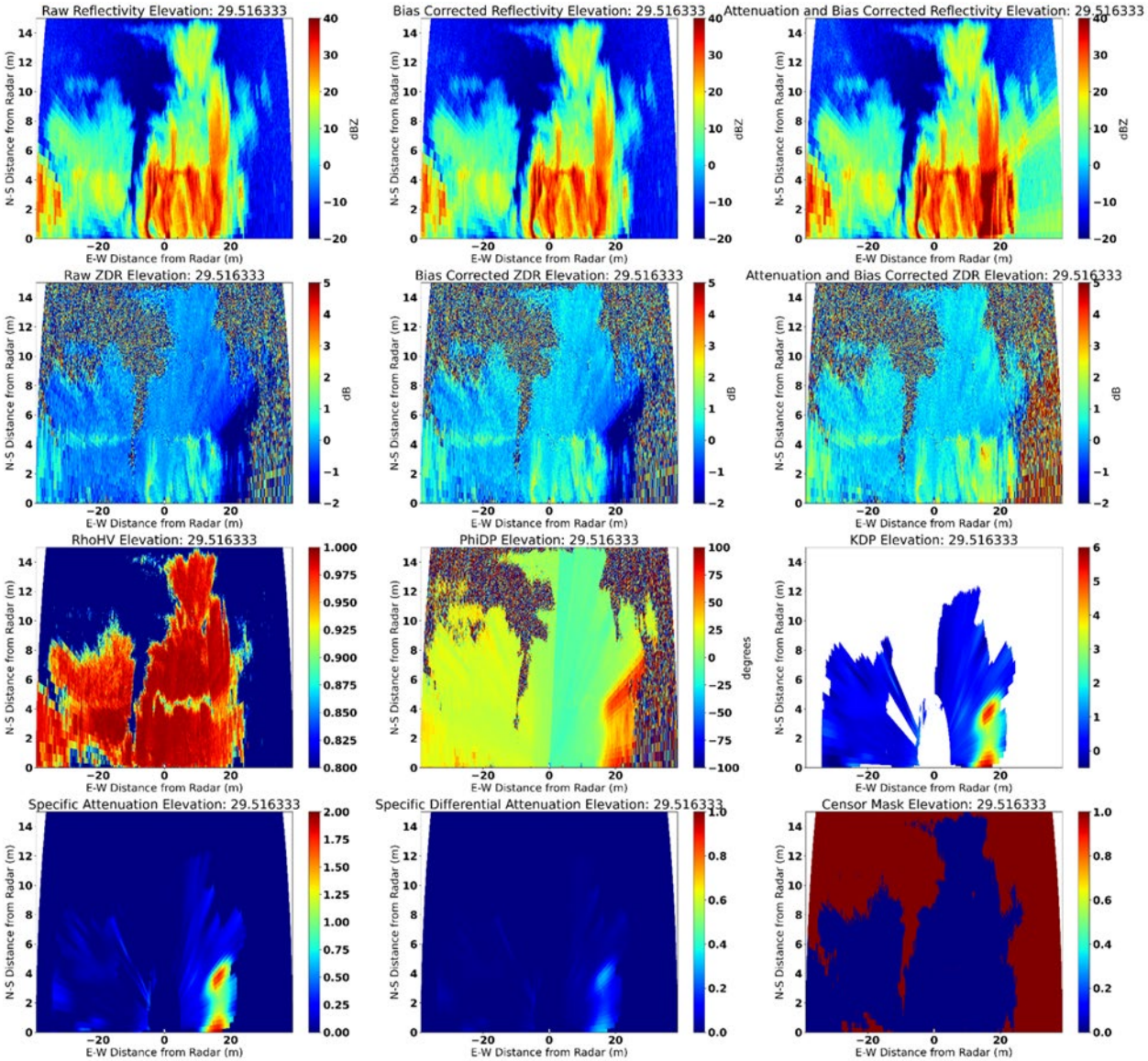

Figure 18. XSACR a1-to-b1-level transformation. Same figure caption as Figure 13 except for the last plot, which displays the censor mask of XSACR.

During TRACER, SACR stands out as the sole ARM radar consistently conducting PPI scans, providing successive horizontal maps of convection evolution. Figure 19 shows boundary-layer convective rolls observed in the TRACER XSACR data, facilitated by biological returns. These signatures are characterized by high ZDR and low RhoHV. In Figure 19, GOES-16 satellite imagery provides additional insight into the development of these convective rolls into clouds a few hours later.

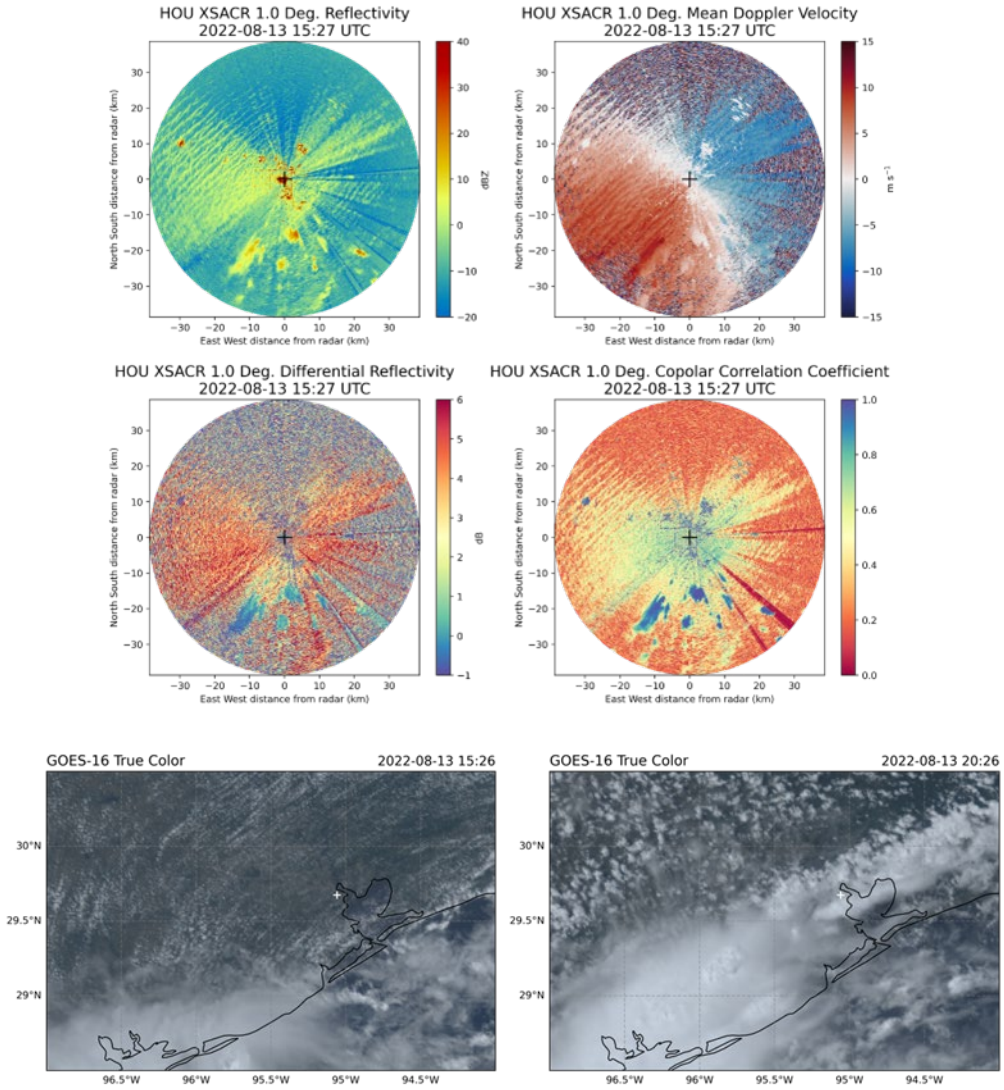

Figure 19. XSACR PPI scans at 1-degree elevation, showing boundary-layer convective rolls before the initiation of convection. GOES-16 satellite images captured at the same time and five hours later also show the development from clouds to storms.

3.2.4 Masks

The XSACR censor mask uses both SNR and RhoHV to differentiate between meteorological and non-meteorological echoes. A SNR threshold of 0.0 dB and a RhoHV threshold of 0.8 were applied. This effectively eliminates a significant amount of noise while preserving cloud edges, as shown in Figure 20. The KaSACR applies a simple SNR censor mask to distinguish between non-meteorological and meteorological echoes. After testing, it was found that a filter for SNR threshold of -5 dB worked well because it removed most of the noise but kept cloud edges intact. An example is shown in Figure 21. However, it was found that this method is less effective in handling second-trip echoes in KaSACR, so caution is advised when interpreting data in the presence of such echoes (Figure 22). Second trip remains challenging to mask out with current methodologies, but a potential alternative approach could involve the application of machine learning methods for feature identification.

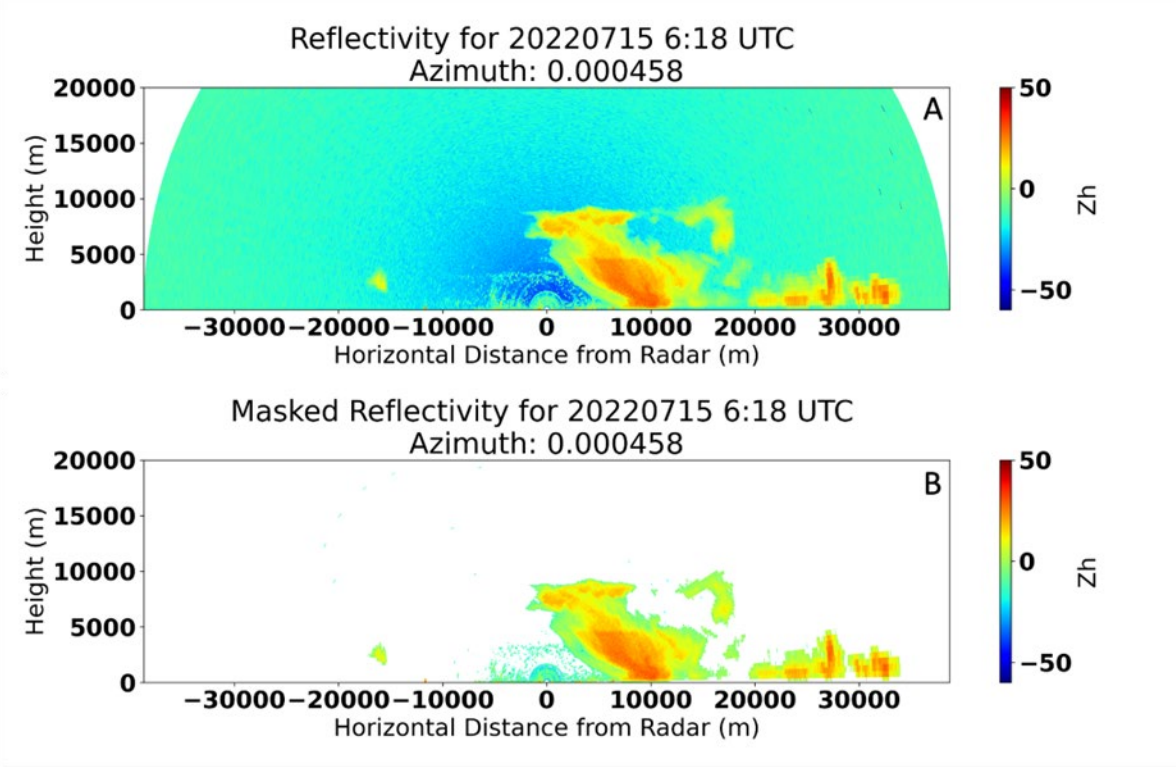

Figure 20. a) Unmasked XSACR reflectivity. b) The same data with the censor mask applied.

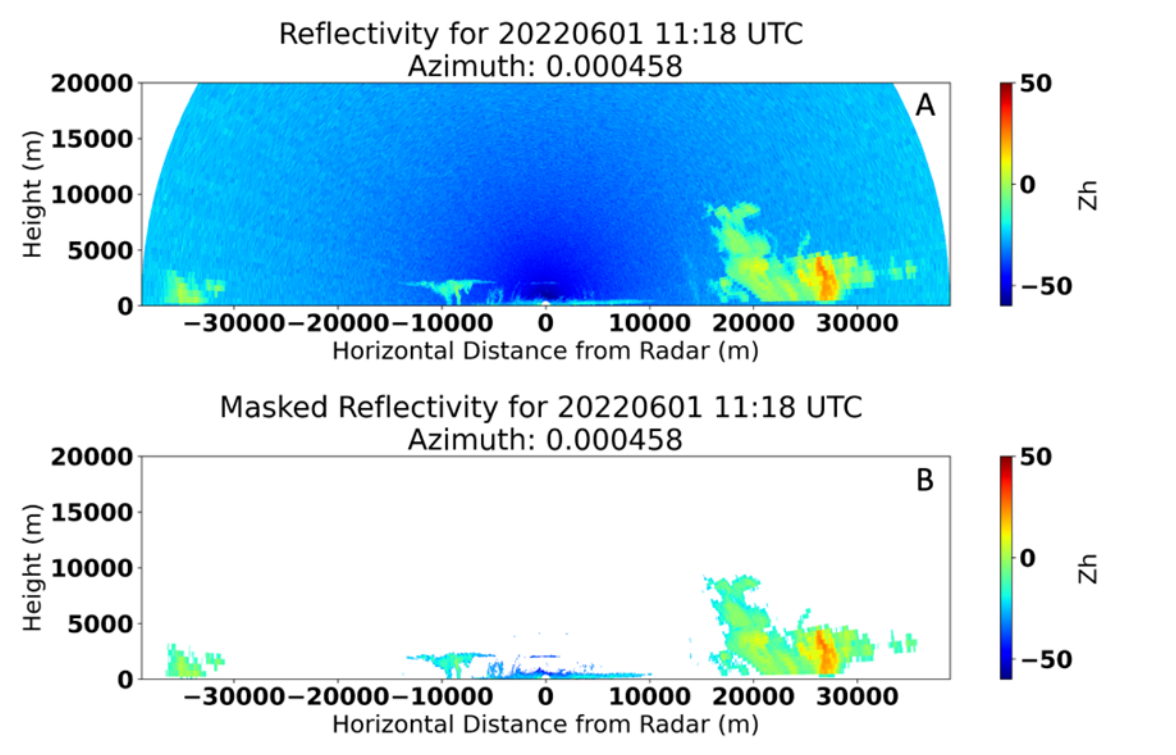

Figure 21. a) An example of the KaSACR reflectivity prior to masking. b) The same data with the censor mask applied.

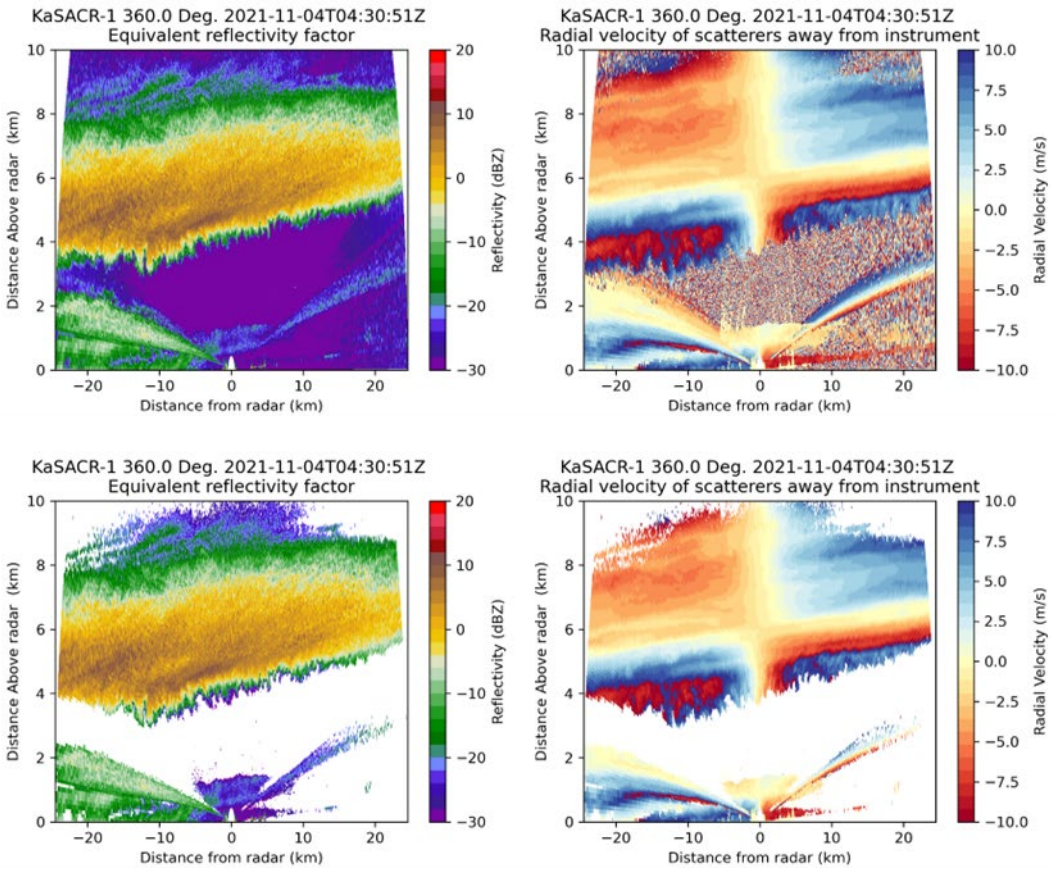

Figure 22. Examples of the KaSACR second-trip features as artificial bands below 3 km in reflectivity (left column) and radial velocity (right column) fields. The upper panels show the a1-level raw data, while the lower panels depict the data with SNR <-5 dB threshold.

3.3 KAZR Data Correction

The estimations of Z_{system_bias} for KAZR general sensitivity (GE) and chirp moderate sensitivity (MD) modes involve two steps. First, the KAZR GE mode Z_{system_bias} is derived through cross-comparison between the $Z_{b1\_corrected}$ of KaSACR and Z_{a1} of KAZR GE mode. Then, Z_{system_bias} of KAZR MD is derived through cross-comparison using $Z_{b1\_corrected}$ of KAZR GE mode.

3.3.1 Z Cross-Comparison between KAZR and KaSACR

The KAZR has three distinct periods of calibration depending on hardware conditions of KAZR and KaSACR as illustrated in Figure 23.

1. The first calibration period: October 1, 2021 to March 20, 2022.
2. The second calibration period: March 21, 2022 to June 30, 2022 (Figure 25).

3. The third calibration period: July 1, 2022 to September 30, 2022. The linearly increasing trend observed from July 1 onwards is attributed to a hardware problem affecting the KAZR. This might be associated with a transmitter drop of about 1 dB starting in June (Figure 24). Two linear fits are applied to the data, one for July 1 to August 31, and one from September 1 to September 30 (Figure 27).

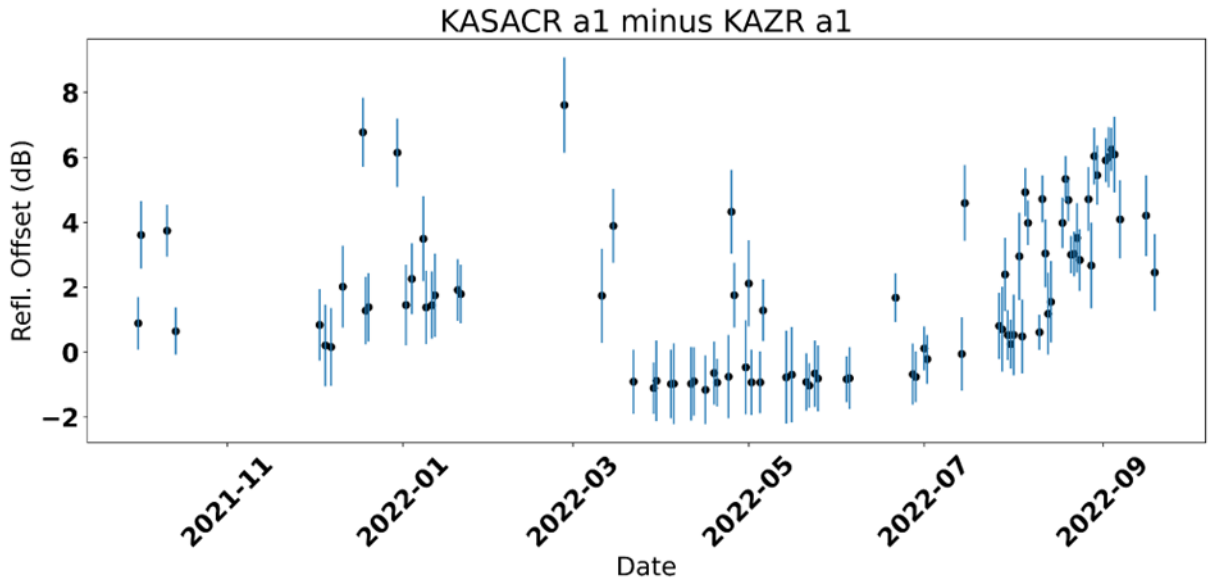

Figure 23. KaSACR a1 data compared to KAZR a1 data, showing three distinct calibration time periods.

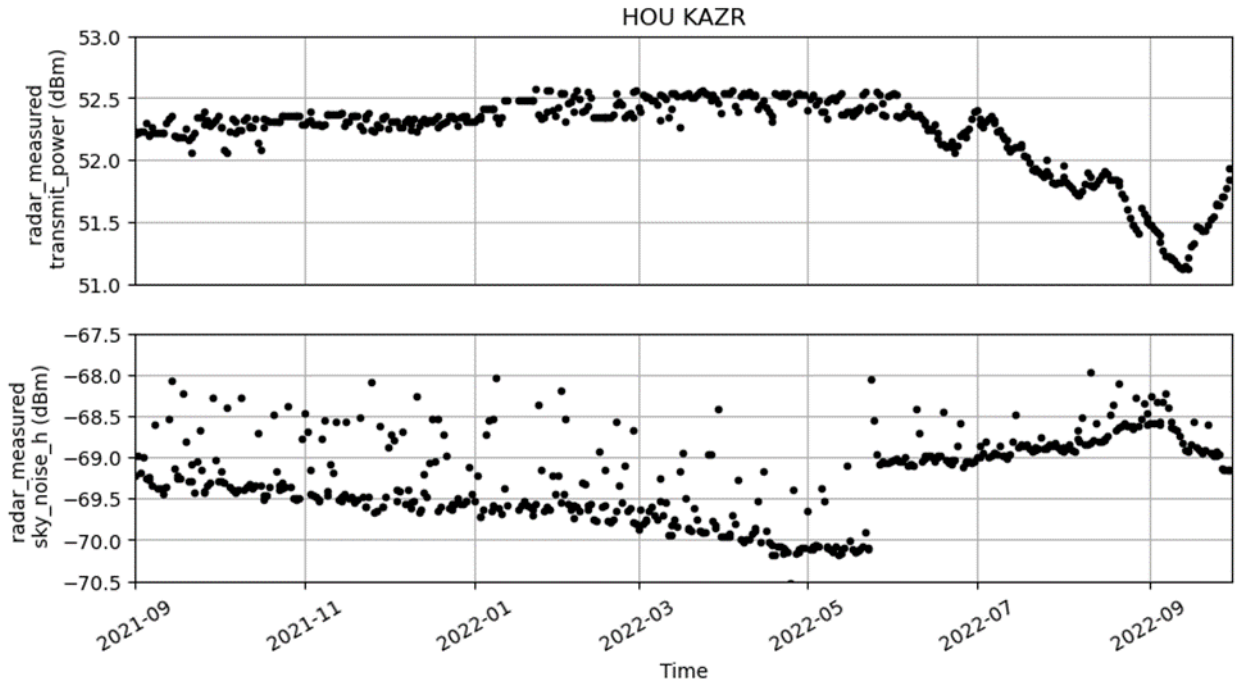

Figure 24. Time series of KAZR transmitter power in dB and of the radar-measured sky noise.

We started the analysis from the second period, spanning March 21 to July 1. The KaSACR $Z_{b1\_corrected}$ was compared with the Z_{a1} of KAZR GE to assess the KAZR GE Z_{system_bias}. The data set was filtered to include only instances where the SNR was greater than 0 dB and the reflectivity was between -5 and 15 dBZ. The result in Figure 25 shows that the KAZR GE Z offset is 1 dB, i.e., KAZR $Z_{b1\_corrected}$ = KAZR Z_{a1} + 1 dB. This period was chosen starting from March, as it aligns with the currently available KaSACR corrected data time frame, determined after the replacement of the low-noise amplifier (LNA) in XSACR.

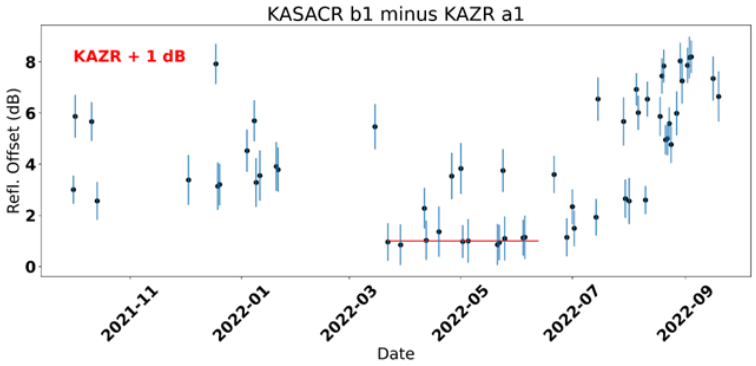

Figure 25. KaSACR b1 reflectivity comparison with KAZR a1 reflectivity during March 21 to July 1, for determining the KAZR reflectivity correction.

Next, we can use the $Z_{b1\_corrected}$ of KAZR to re-compare Z_{a1} of KaSACR to find the KaSACR Z_{system_bias} from Oct 2021 to March 2022, which could not be obtained due to XSACR hardware issues. From this, Figure 26 shows that KaSACR and KAZR agreed well, with only a -0.4 dB offset for this period.

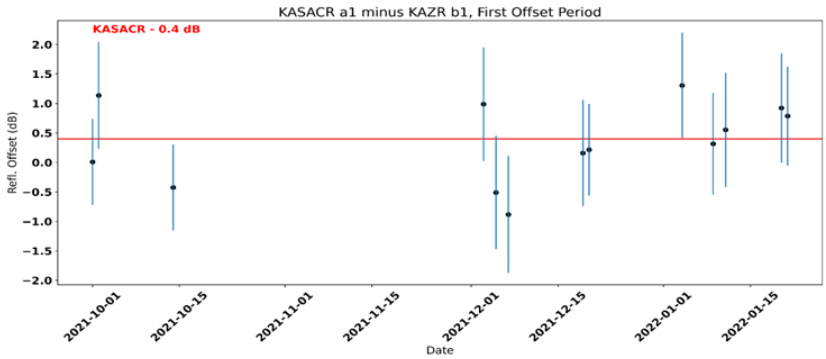

Figure 26. KaSACR a1 reflectivity compared with KAZR b1 reflectivity for the first offset period.

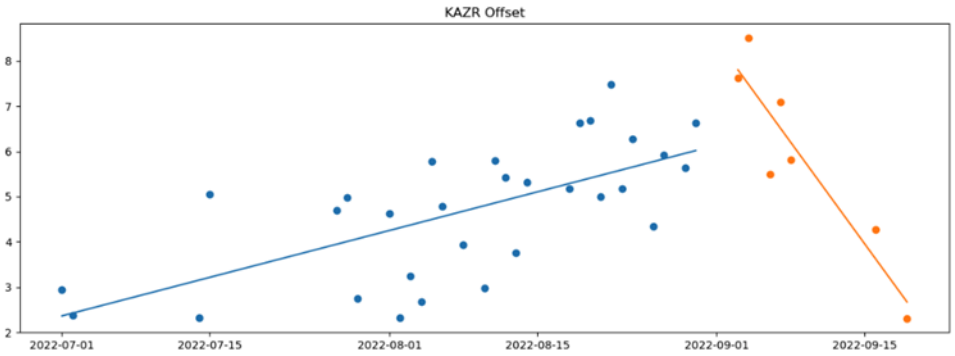

Figure 27. Linear offsets applied to the KAZR GE reflectivity.

Once all corrections are applied, the $Z_{b1\_corrected}$ of KaSACR and $Z_{b1\_corrected}$ of KAZR GE agree well, with the mean difference throughout the campaign now near 0 dB (Figure 28).

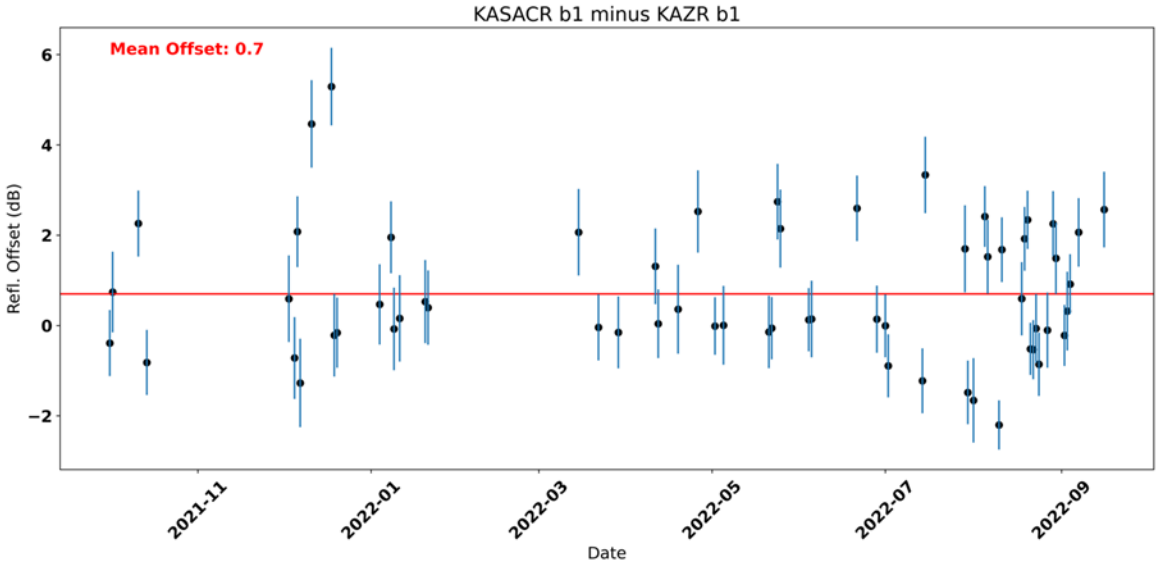

Figure 28. KaSACR $Z_{b1\_corrected}$ comparison with KAZR $Z_{b1\_corrected}$.

3.3.2 MD-GE Mode Comparison

Next, we compared the reflectivity between the KAZR GE mode and MD mode, using a data filter with an SNR > 0 dB and reflectivity values between -5 and 15 dBZ. This comparison will show us how well the pulse compression filter fits throughout the campaign. Figure 29 shows that in the first month of the campaign the filter was re-evaluated, and the difference between the two modes dropped from 1.5 dB to 1 dB, where it stayed for the rest of the campaign.

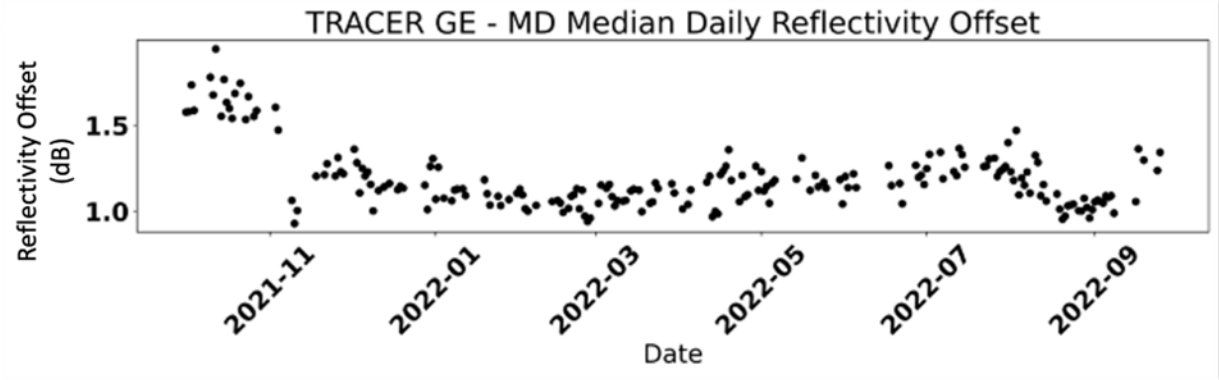

Figure 29. KAZR GE a1-level reflectivity compared with the KAZR MD a1-level reflectivity.

After the KAZR GE data is corrected by 1 dB and the linear offset during the last two months of the campaign found from the KAZR GE versus KaSACR comparison is applied, we can recreate this comparison between the GE and MD modes, which is shown in Figure 30.

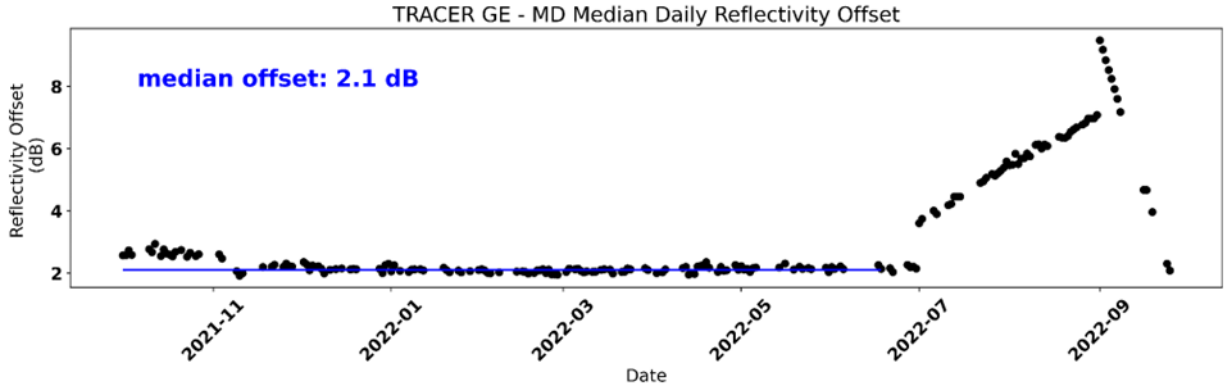

Figure 30. KAZR GE b1-level reflectivity compared with the uncorrected KAZR MD a1-level data.

From here, we found the MD offset of 2.1 dB and the linear offsets from GE and were able to correct the MD mode data as well, shown in Figure 31. After both modes were corrected, the reflectivity agreed very well, with a mean difference of just 0.05 dB.

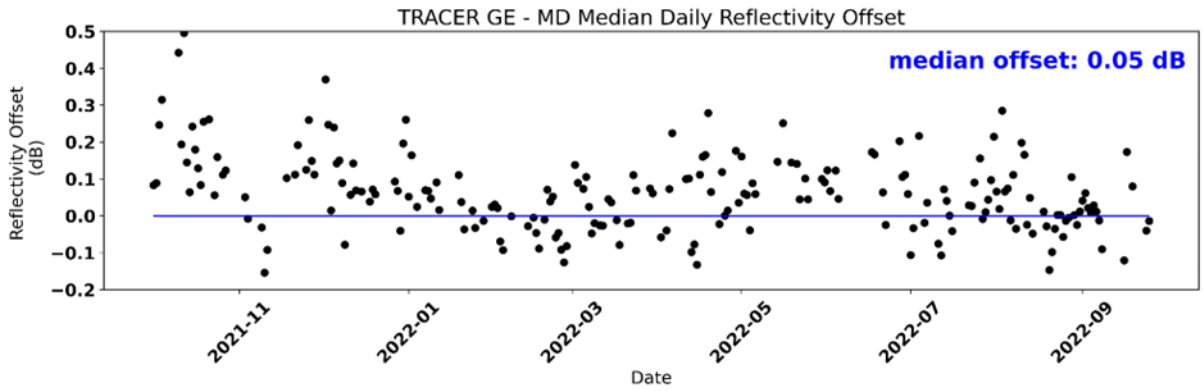

Figure 31. KAZR GE b1 and KAZR MD b1 reflectivity comparisons, showing the data sets now agree well.

3.3.3 Wet Radome Discussion

When comparing KAZR Za1 data with the calibrated RWP data at 500-800 m height (Figure 32), the reflectivity difference between these two instruments varied with time. In the initial stage of precipitation, the Z difference was nearly zero. As the precipitation persisted with Z greater than 30 dBZ, a gradual increase in reflectivity discrepancy between KAZR and RWP became evident over time, reaching up to 10 dB. However, this Z difference between KAZR and RWP continued to be observed even as the rainfall intensity dropped and the RWP Z decreased to 15 dBZ, when hydrometer attenuations is smaller than 1 dB. Consequently, the Z difference appears to be attributed to factors beyond hydrometeor attenuation. The Z difference persists over time during ongoing rainfall, leading us to suspect that it is associated with the accumulated rainfall on the radome, known as the wet-radome effect. The time-dependent Z differences caused by the wet-radome effect were not corrected in the current b1 data set, since it depends on multiple factors including rainfall intensity, duration, and wind conditions. Please be aware of this effect when directly applying intercomparison between KAZR and disdrometer data.

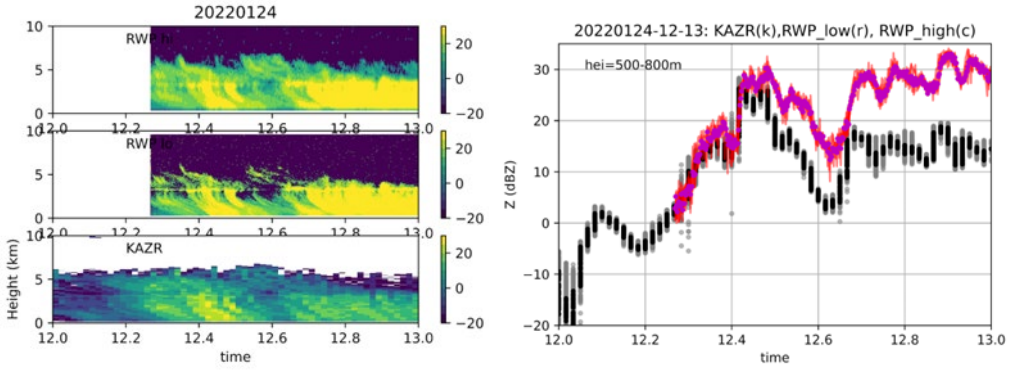

Figure 32. The reflectivity intercomparison between the calibrated RWP data (provided by Dr. Christopher Williams) and the KAZR Z_{a1} raw data on January 24, 2022.

3.3.4 Z Cross-Comparison between KAZR and Disdrometers

The KAZR a1-level reflectivity is compared with the VDISQUANTS reflectivity after correcting the attenuations of gas, rain, and wet radome (Figure 33, orange). More details on how to obtain reflectivity offsets from LDQUANTS using the wet-radome attenuation technique are provided in Appendix B. This is plotted alongside the KaSACR b1-minus-KAZR a1 reflectivity comparisons (Figure 33, blue). Both reflectivity offsets show a similar trend and agree well with each other within 1 dB over the full campaign. This is within the expected uncertainty, as the disdrometer data has an estimated 2 dB of uncertainty from both the instrument itself as well as the calculation of reflectivity from the drop size distribution, and the radar comparison also has 2 dB of uncertainty.

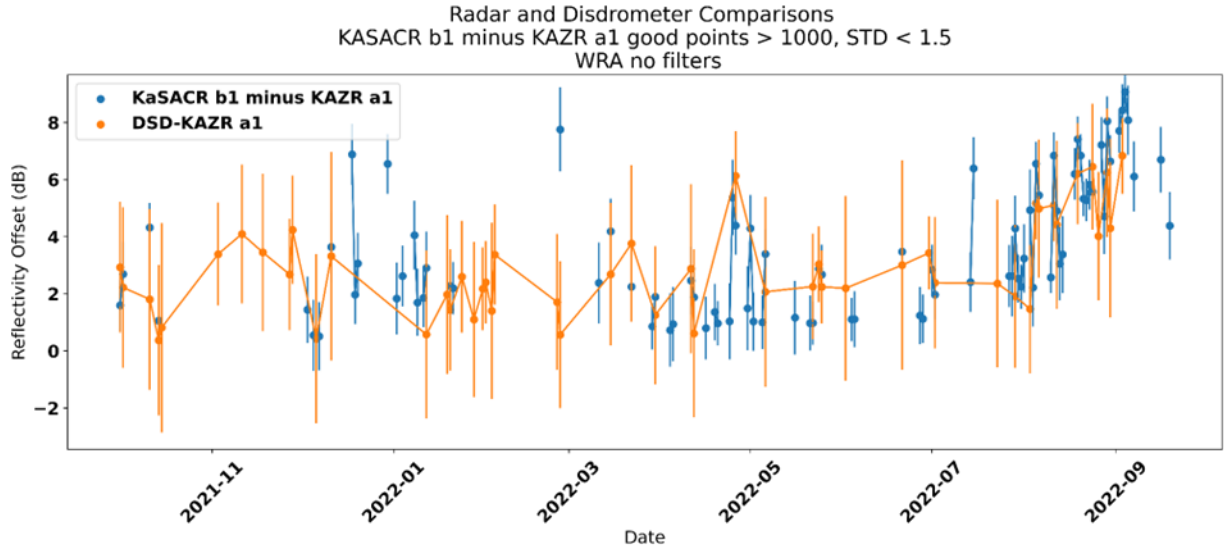

Figure 33. DSD versus KAZR a1 and KASACR b1 versus KAZR a1 data showing relative agreement between the two methods.

3.4 Z Cross-Comparison

The KAZR mask (Figure 34) is determined by the velocity texture. Note that KAZR deployed in TRACER is single polarization and does not provide linear depolarization ratio (LDR) fields commonly used for filtering out biological echoes.

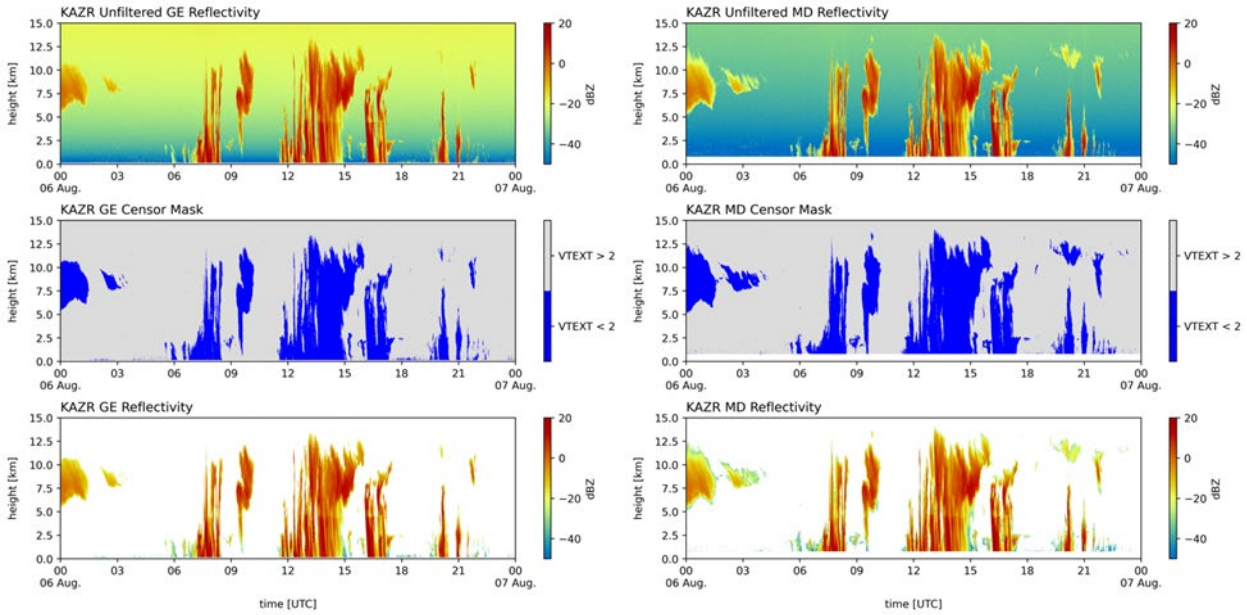

Figure 34. KAZR mask for GE and MD modes (left, right columns). The rolls from top to bottom: unfiltered Z, cloud censor mask, and Z after mask.

4.0 Description of Data Files

A list of relevant variables in the b1-level radar datastream is provided, with the variables arranged alphabetically.

Key
New variable calculated in b1 data
Correction applied
New variable and correction applied

CSAPR2 File Contents at b1-level	
Moments	
attenuation_corrected_differential_reflectivity	Differential reflectivity (ZDR) with attenuation correction and offset applied. $ZDR_{b1\_corrected} = ZDR_{a1} + ZDR_{system\_bias} + ZDR_{attenuation}$
attenuation_corrected_differential_reflectivity_lag_1	Differential reflectivity (ZDR) at lag 1 with attenuation correction and offset applied.
attenuation_corrected_reflectivity_h	Horizontal reflectivity with attenuation correction and offset applied. $Z_{b1\_corrected} = Z_{a1} + Z_{system\_bias} + Z_{attenuation}$
copol_correlation_coeff	Copolar correlation coefficient (RhoHV).
differential_phase	Differential propagation phase shift.
differential_reflectivity	Differential reflectivity (ZDR) with offset applied.

CSAPR2 File Contents at b1-level	
	$ZDR_{a1} + ZDR_{system\_bias}$
differential_reflectivity_lag_1	Differential reflectivity estimated at lag 1 with offset applied.
mean_doppler_velocity	Radial mean doppler velocity, positive for motion away from the radar.
mean_doppler_velocity_v	Radial mean doppler velocity in the vertical channel, positive for motion away from the radar.
normalized_coherent_power	Normalized coherent power (SQI).
normalized_coherent_power_v	Normalized coherent power, vertical channel.
reflectivity	Equivalent reflectivity factor with offset applied. $Z_{a1} + Z_{system\ bias}$
reflectivity_v	Equivalent reflectivity factor, vertical channel.
signal_to_noise_ratio_copolar_h	Signal-to-noise ratio (SNR), horizontal channel.
signal_to_noise_ratio_copolar_v	Signal-to-noise ratio, vertical channel.
specific_attenuation	Specific attenuation at each bin. Integral of this is applied for correction to attenuation_corrected_reflectivity_h (Ah)
specific_differential_attenuation	Specific differential attenuation at each bin. Integral of this is applied for correction to attenuation_corrected_differential_reflectivity A_{DP})
specific_differential_phase	Specific differential phase (KDP). Calculated using reflectivity, differential phase, and range.
spectral_width	Spectral width.
spectral_width_v	Spectral width, vertical channel.
Masks	
censor_mask	Censor mask. See variable details in the files for flags and meanings.
classification_mask	Classification mask.

XSACR File Contents at b1-level	
Moments	
attenuation_corrected_differential_reflectivity	Rainfall attenuation-corrected differential reflectivity with attenuation correction and offset. $ZDR_{b1\_corrected} = ZDR_{a1} + ZDR_{system\_bias} + ZDR_{attenuation}$
attenuation_corrected_reflectivity_h	Rainfall attenuation-corrected reflectivity, horizontal channel, with attenuation correction and offset applied. $Z_{b1\ corrected} = Z_{a1} + Z_{system\ bias} + Z_{attenuation}$
copol_correlation_coeff	Copolar correlation coefficient (RhoHV).
differential_phase	Differential propagation phase shift.
differential_reflectivity	Differential reflectivity (ZDR) with offset applied. $ZDR_{a1} + ZDR_{system\_bias}$

XSACR File Contents at b1-level	
mean_doppler_velocity	Radial mean Doppler velocity, positive motion away from the instrument.
reflectivity	Equivalent reflectivity factor with offset applied. $Z_{a1} + Z_{system\ bias}$
signal_to_noise_ratio_copolar_h	Signal-to-noise ratio (SNR), horizontal channel.
signal_to_noise_ratio_crosspolar_v	Signal-to-noise ratio, cross-polar for vertical channel.
specific_attenuation	Specific attenuation at each bin. Integral of this is applied for correction to attenuation_corrected_reflectivity_h
specific_differential_attenuation	Specific differential attenuation at each bin. Integral of this is applied for correction to attenuation_corrected_differential_reflectivity
specific_differential_phase	Specific differential phase (KDP), calculated using reflectivity, differential phase, and range fields.
spectral_width	Spectral width.
Masks	
censor_mask	Bit mask 0: no mask 1: SNR < 0 2: RhoHV < 0.8

KASACR File Contents at b1 level	
Moments	
co_to_crosspol_correlation_coeff	Copolar to cross-polar correlation coefficient (RhoXH).
crosspolar_differential_phase	Cross-polar propagation phase shift.
linear_depolarization_ratio_v	Linear depolarization ratio, vertical channel.
mean_doppler_velocity	Radial mean Doppler velocity, positive for motion away from the radar.
reflectivity	Equivalent reflectivity factor, with offset applied.
signal_to_noise_ratio_copolar_h	Signal-to-noise ratio (SNR), horizontal channel.
signal_to_noise_ratio_crosspolar_v	Signal-to-noise ratio, vertical channel.
spectral_width	Spectral width.
Masks	
censor_mask	Bit mask 1: SNR < -5
Clutter_mask	1: Z>10 dBZ, SNR>0 dB, absolute Vr <0.1

KAZR File Contents at b1-level	
Moments	
linear_depolarization_ratio	All values set to nan. This variable is not present in this KAZR.
mean_doppler_velocity	Radial mean Doppler velocity, positive for motion away from the radar.
mean_doppler_velocity_crosspolar_v	All values set to nan. This variable is not present in this KAZR.
reflectivity	Equivalent reflectivity factor, with offset applied.
reflectivity_crosspolar_v	All values set to nan. This variable is not present in this KAZR.
signal_to_noise_ratio_copolar_h	Signal-to-noise ratio (SNR), horizontal channel.
signal_to_noise_ratio_crosspolar_v	All values set to nan. This variable is not present in this KAZR.
spectral_width	Spectral width.
spectral_width_crosspolar_v	All values set to nan. This variable is not present in this KAZR.
Masks	
censor_mask	Bit mask 0: no mask 4: velocity texture threshold of 2.0 applied based on mean_doppler_velocity after correction.

5.0 References

Bharadwaj, N, K Widener, A Lindenmaier, and V Venkatesh. 2013. "Calibration System For ARM Radars." American Meteorological Society 36th Conference on Radar Meteorology.

Chandrasekar, L, N Baldini, N Bharadwaj, and PL Smith. 2015. "Calibration procedures for global precipitation-measurement ground-validation radars." *URSI Radio Science Bulletin* 2015(355): 45–73, https://doi.org/10.23919/URSIRSB.2015.7909473

CSU-Radarmet/CSU_RadarTools. 2020. CSU Radar Meteorology Group. https://github.com/CSURadarmet/CSU_RadarTools

Deng, M, SE Giangrande, MP Jensen, K Johnson, CR Williams, JM Comstock, Y Feng, A Matthews, IA Lindenmaier, TG Wendler, M Rocque, A Zhou, Z Zhu, E Luke, and D Wang. 2023. "Calibration of ARM TRACER Cloud Radar Observations Using Disdrometer Measurements under Wet-Radome Conditions." Submitted to *Journal of Atmospheric and Oceanic Technology*.

Feng, Z, J Hardin, HC Barnes, J Li, LR Leung, A Varble, and Z Zhang. 2023. "PyFLEXTRKR: a flexible feature tracking Python software for convective cloud analysis." *Geoscientific Model Development* 16(10): 2753–2776, https://doi.org/10.5194/gmd-16-2753-2023

Hardin, J, SE Giangrande, and A Zhou. 2020. Laser Disdrometer Quantities (LDQUANTS) and Video Disdrometer Quantities (VDISQUANTS) Value-Added Products Report. U.S. Department of Energy. DOE/SC-ARM-TR-221, https://doi.org/10.2172/1808573

Helmus JJ, and SM Collis. 2016. "The Python ARM Radar Toolkit (Py-ART), a Library for Working with Weather Radar Data in the Python Programming Language." *Journal of Open Research Software* 4(1): e25, https://doi.org/10.5334/jors.119

Hubbert, J, and VN Bringi. 1995. "An iterative filtering technique for the analysis of copolar differential phase and dual-frequency radar measurements." *Journal of Atmospheric and Oceanic Technology* 12(3): 643–648, https://doi.org/10.1175/1520-0426(1995)012<0643:AIFTFT>2.0.CO;2

Hunzinger, A, JC Hardin, N Bharadwaj, A Varble, and A Matthews. 2020. "An extended radar relative calibration adjustment (eRCA) technique for higher-frequency radars and range–height indicator (RHI) scans." *Atmospheric Measurement Techniques* 13(6): 3147–3166, https://doi.org/10.5194/amt-13-3147-2020

Lamer, K, P Kollias, EP Luke, BP Treserras, M Oue, and B Dolan. 2023. "Multisensor Agile Adaptive Sampling (MAAS): A Methodology to Collect Radar Observations of Convective Cell Life Cycle." *Journal of Atmospheric and Oceanic Technology* 40(11): 1509–1522, https://doi.org/10.1175/JTECH-D-23-0043.1

Silberstein DS, DB Wolff, DA Marks, D Atlas, and JL Pippitt. 2008. "Ground clutter as a monitor of radar stability at Kwajalein, RMI." *Journal of Atmospheric and Oceanic Technology* 25(11): 2037–2045, https://doi.org/10.1175/2008JTECHA1063.1

Wolff, DB, DA Marks, and WA Petersen. 2015. "General Application of the Relative Calibration Adjustment (RCA) Technique for Monitoring and Correcting Radar Reflectivity Calibration." *Journal of Atmospheric and Oceanic Technology* 32(3): 496–506, https://doi.org/10.1175/JTECH-D-13-00185.1

Appendix A

Engineer Calibration

The engineering team performed standard hardware calibrations through laboratory calibration, corner reflector calibration, and radar pointing and leveling evaluation in the field. The following introduces the calibration results in the early stage of the experiment. This content is by Tim Wendler.

A.1 Corner Reflector

The corner reflector calibration is one of the methods we use to do an end-to-end calibration. Given the transmit power of the radar, we bounce a signal off an elevated trihedral reflector at a known distance R from the radar. This reflector has a known radar cross-section (RCS), so we know how much power P_r is expected to reflect to the radar from this reflector as defined by its geometry (Bharadwaj et al. 2013, Chandrasekar et al. 2014). For a trihedral corner reflector with edge length l, and free-field wavelength λ, we can calculate the maximum RCS as

$$\sigma_{cr} = \frac{\pi l^4}{3\lambda^2} \tag{A1}$$

This well-defined RCS allows us to exploit the canonical radar equation to derive a corner reflector calibration constant C_{cr}:

$$C_{cr} = 10\left\{\frac{1}{\pi^5 |K_w|^2}\left(\frac{2}{c\tau}\right)\left(\frac{8ln\ln 2}{\pi\theta\varphi}\right)\left(\frac{\sigma_{cr}}{P_r R^4}\right)\lambda^4 10^{18} l_f l_p l_m\right\} \tag{A2}$$

During TRACER, corner reflector calibration was performed successfully towards the beginning of the campaign (Figure 35). The radar constant offset is small at 0.32 dB. There are challenges for performing the corner reflector calibration, such as the pointing issues and the surrounding conditions. The successful calibration was most likely due to our technician being able to focus on pointing the reflector very accurately back toward the SACR. The surrounding runways in the airport also cause errors for the calibration (Figure 36).

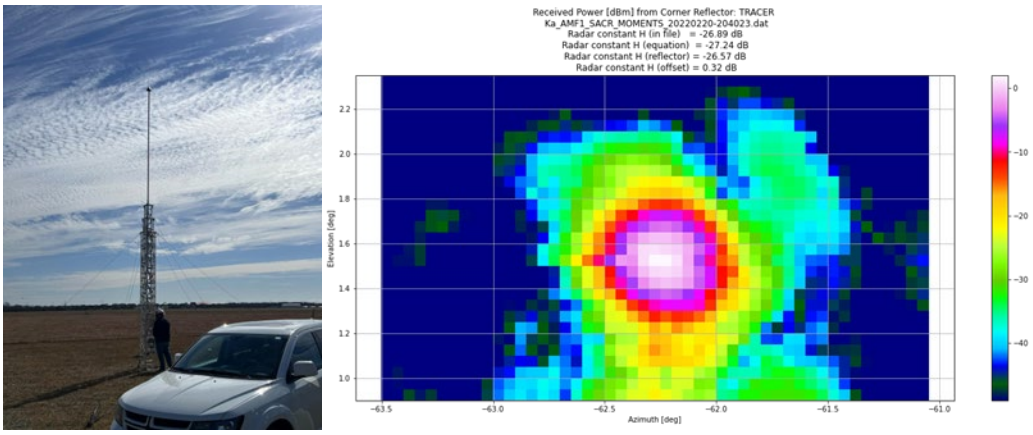

Figure 35. a) Corner reflector at TRACER: This shows the lower telescoping metallic truss section before extension with the fiberglass pole on top connected to the trihedral to minimize the influence of RCS. b) Most successful Ka-Band corner reflector raster scan results from TRACER with the three important constants reported above and the "observable offset" being very small (0.32dB).

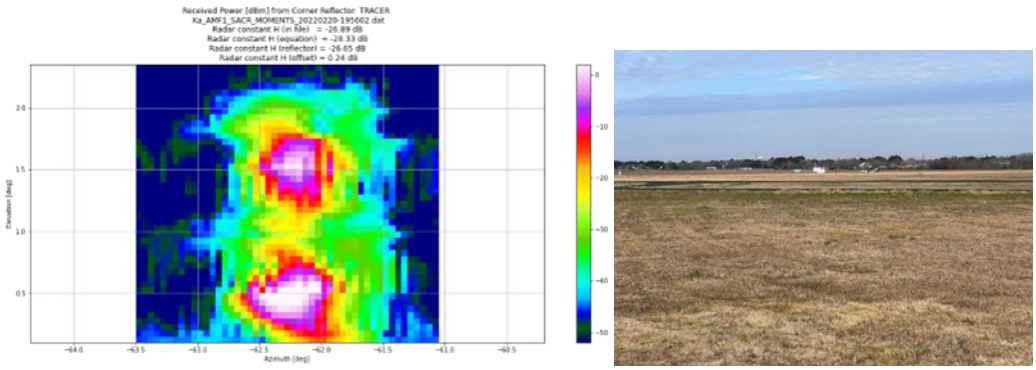

Figure 36. a) The challenges of the SACR corner reflector calibration caused by the "mirror-like" effects from the two runways directly between the SACR and the trihedral. b) A look at the corner reflector from the SACR roof. The two runways produce obvious multipath effects seen in the results.

A.2 Solar Calibration for Radar Pointing and Pedestal Base Leveling

Here is an example of one of the initial Ka- and X-band H/V channel solar calibration scans used for orientation calibration (Figure 37). Later, we used the obvious difference in sky noise floor to correct inherent receiver imbalance. Measurements of pedestal base level performed by Vagner Castro on site indicate the base was within one-tenth of a degree of being level (Figure 37).

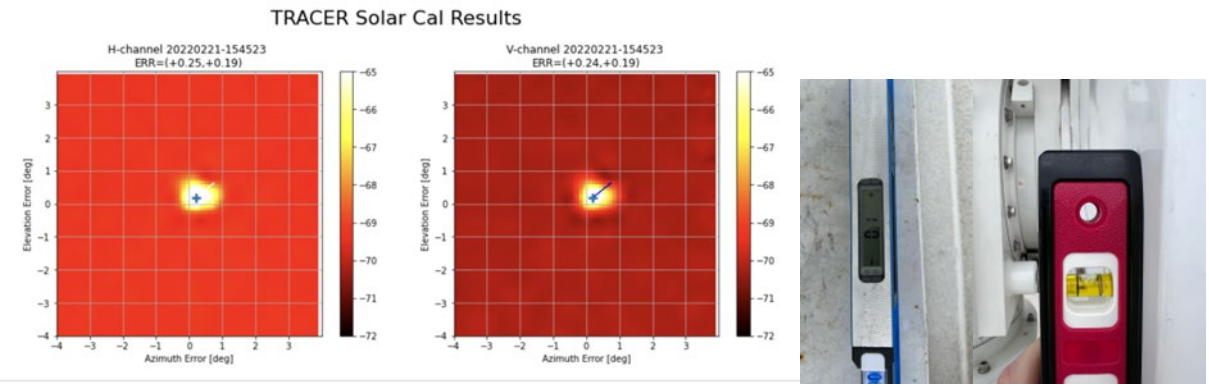

Figure 37. Examples of the solar calibration of horizontal and vertical channels result from the SACR and the pedestal base level calibration.

Appendix B

The KAZR Wet-Radome Calibration Method

B.1 KAZR Wet-Radome Attenuation Correction

The two-way attenuation associated with radome wetting, i.e., the wet-radome attenuation (WRA), mainly depends on the thickness of the water film on the radome, which in turn is a function of the rain rate (RR). WRA can be more than 10 dB in moderate rain of 5 mm hr^{-1} (Deng et. al. 2024). Disdrometer-based calibration methods attempt to estimate the offset between the radar-measured near surface and disdrometer-estimated Ze (*Dze*) with the inherent assumption that the disdrometer estimates are truth, and thus related to the radar constant as:

$$D_{Ze} = Ze_{\mathrm{Vdis}} - Ze_{\mathrm{meas}} = C \tag{B1}$$

Figure 38a shows that the disdrometer-estimated Ze and KAZR-measured Ze at 500 meters and their difference as a function of rain rate for the observation on September 3. The increased trend of the *Dze* with rain rate in Figure 38b is due to the WRA dependence of rain rate. As Figure 38b demonstrates that there is a quasi-linear correlation between Dze and RR in logarithmic space, a weighted linear least-square fitting of the $Dze_{\ with}\ RR$ in logarithm in Equation (B1) is performed:

$$D_{ze} = a + b\ log\ (RR) \tag{B2}$$

The fitted slope *b* is estimated to be around 8.

B.2 KAZR WRA Calibration Technique

KAZR Ze after the WRA correction should be parallel with the disdrometer-estimated Ze as shown in Figure 38c on the right. Figure 39 shows the one-to-one comparison of Ze after WRA correction with disdrometer estimates. The bias between them is the calibration offset. The calibration offset is for around 7.3 dB in a1 data. Users should be cautious with the b1 data calibration uncertainty. Details of the WRA calibration technique are in Deng et al. 2023.

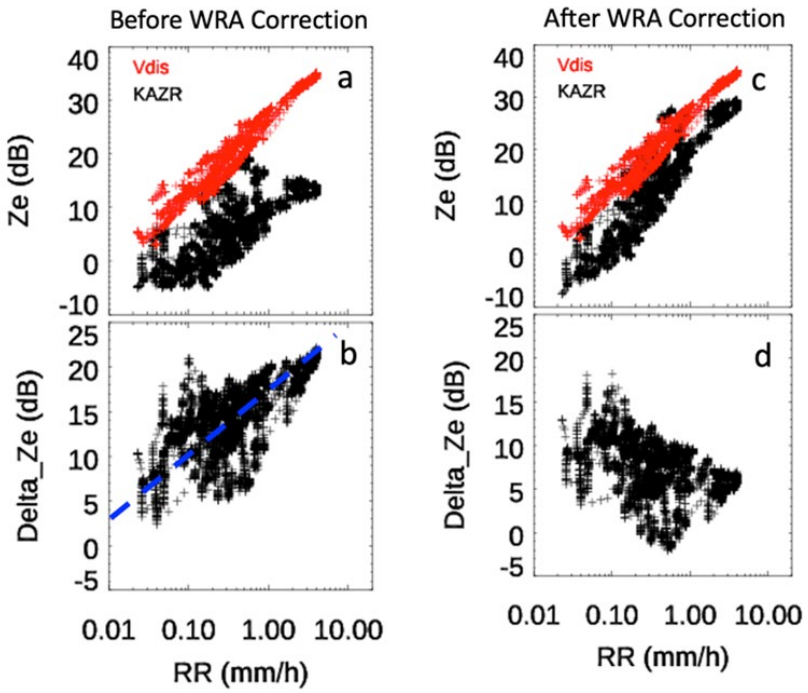

Figure 38. a) Scatter plot of KAZR-measured Ze (black cross) at 500 m after gas and rain attenuation correction and VDISQUANTS-estimated Ze (red cross) as a function of rain rate (*RR*). b) Difference between KAZR-measured Ze and VDISQUANTS-estimated Ze (Dze) as a function of *RR*. The linear relation between Dze and *R* is fitted with Equation 1 with a slope *b* at 8. c) and d) are results for the corrected KAZR Ze with the fitted WRA relation.

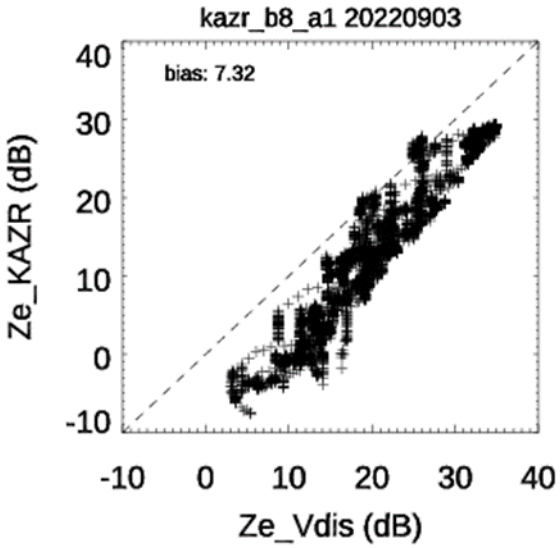

Figure 39. The one-to-one comparison of KAZR-measured Ze after WRA correction with disdrometer estimate for a1 data. The calibration bias in a1 data is about 7.32 dB.

www.arm.gov